



THE UNIVERSITY *of* EDINBURGH

Edinburgh Research Explorer

Gloria Knolls Slide: a prominent submarine landslide complex on the Great Barrier Reef margin of north-eastern Australia

Citation for published version:

PUGA-BERNABEU, ANGEL, Beaman, RJ, Webster, JM, Thomas, A & Jacobsen, G 2017, 'Gloria Knolls Slide: a prominent submarine landslide complex on the Great Barrier Reef margin of north-eastern Australia' *Marine Geology*, vol. 385, pp. 68-83. DOI: 10.1016/j.margeo.2016.12.008

Digital Object Identifier (DOI):

[10.1016/j.margeo.2016.12.008](https://doi.org/10.1016/j.margeo.2016.12.008)

Link:

[Link to publication record in Edinburgh Research Explorer](#)

Document Version:

Peer reviewed version

Published In:

Marine Geology

Publisher Rights Statement:

© 2016 Elsevier B.V. All rights reserved.

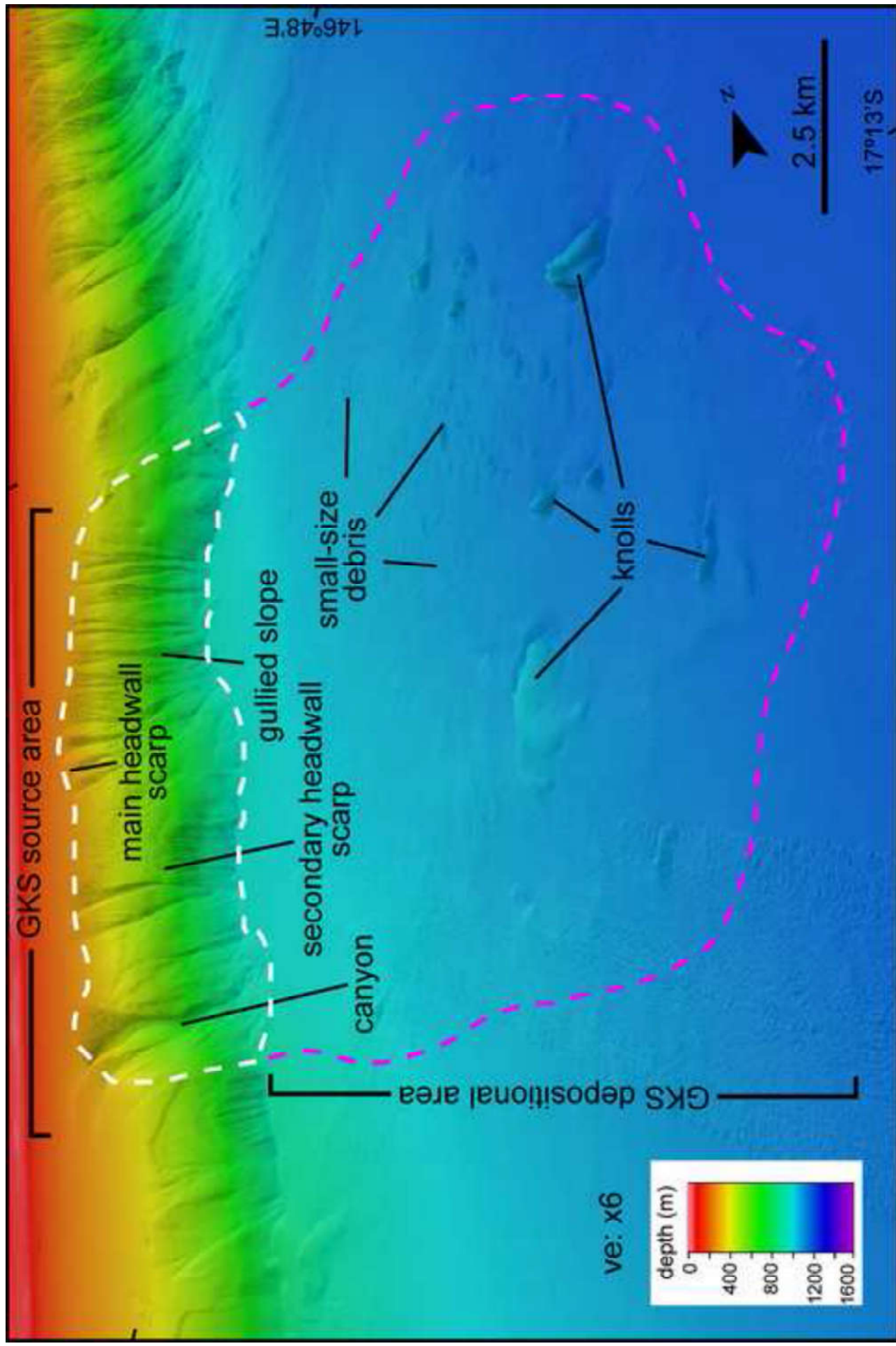
General rights

Copyright for the publications made accessible via the Edinburgh Research Explorer is retained by the author(s) and / or other copyright owners and it is a condition of accessing these publications that users recognise and abide by the legal requirements associated with these rights.

Take down policy

The University of Edinburgh has made every reasonable effort to ensure that Edinburgh Research Explorer content complies with UK legislation. If you believe that the public display of this file breaches copyright please contact openaccess@ed.ac.uk providing details, and we will remove access to the work immediately and investigate your claim.





The GKS is the largest landslide complex on the Great Barrier Reef margin

Distinctive cluster of 8 knolls and over 70 small debris blocks in the distal area

The timing of emplacement of the GKS was at least before 302 ka

Failure process includes 3 events spreading from the lower slope to the upper slope

Cold-water coral community identified on the largest slide knolls

1 **Gloria Knolls Slide: a prominent submarine landslide complex on the Great**
2 **Barrier Reef margin of north-eastern Australia**

3
4
5 Ángel Puga-Bernabéu ^{a,c}, Robin J. Beaman ^b, Jody M. Webster ^c, Alex L. Thomas ^d, Geraldine
6 Jacobsen ^e

7
8 ^a Departamento de Estratigrafía y Paleontología, Universidad de Granada, 18002 Granada,
9 Spain

10 ^b College of Science and Engineering, James Cook University, PO Box 6811, Cairns, QLD
11 4870, Australia

12 ^c Geocoastal Group, School of Geosciences, The University of Sydney, NSW 2006, Australia

13 ^d School of Geosciences, The University of Edinburgh, Edinburgh EH9 3FE, UK

14 ^e Institute for Environmental Research, Australia Nuclear Science and Technology
15 Organisation, Locked Bag 2001, Kirrawee, NSW 2232, Australia

16
17 **Abstract**

18 We investigate the Gloria Knolls Slide (GKS) complex on the Great Barrier Reef margin of
19 north-eastern Australia, the largest extant mixed carbonate-siliciclastic province in the world.
20 Based on the most complete bathymetric and sub-bottom profile datasets available for the
21 region, we describe the main surface and subsurface geomorphologic characteristics of this
22 landslide complex. The GKS forms a 20 km along-slope and 8 km across-slope indentation in
23 the margin, extending from 250 to 1350 m depth, and involves a volume of 32 km³ of
24 sediment remobilized during three events. Three main seafloor terrains can be distinguished
25 based on seafloor morphology: a source area, a proximal depositional area and a distal
26 depositional area. The source area includes a main headwall scarp with a maximum height of
27 830 m and a secondary scarp at 670 m depth. The proximal depositional area is flat and
28 smooth, and lacks debris exposed on the seafloor. The distal depositional area has a
29 hummocky surface showing a distinctive cluster of eight knolls and over 70 small debris
30 blocks. A dredge sample from the top of the largest knoll at a depth of 1170 m reveals the
31 presence of a cold-water coral community. In the sub-bottom profiles, the mass-transport
32 deposits in the GKS are identified below the background sediment drape as partially confined,
33 wedge-shaped bodies of mostly weak amplitude, transparent reflectors in the proximal

34 depositional area; and more discontinuous and chaotic in the distal depositional area. The
35 failed sediment slabs of the GKS were evacuated, transported and disintegrated downslope in
36 three events following a sequential failure process spreading successively from the lower
37 slope to the upper slope. The first event initiated at the lower slope at the depth of the
38 secondary scarp, moved downslope and disintegrated over the basin floor leaving coherent
39 blocks. The subsequent second and third events were responsible for the formation upslope of
40 the main scarp in the GKS. The timing of emplacement of the first GKS event, constrained by
41 radiometric age of fossil biota from the surface of the largest slide block, was at least before
42 302 ± 19 ka. The presence of alternating mixed carbonate and siliciclastic lithologies that build
43 the slope might have played an important role as a preconditioning factor in this region.
44 Preliminary estimations suggest that unusually large seismic events were the most likely
45 triggering mechanism for the GKS. This work contributes to the understanding of large mass-
46 movement deposits in mixed carbonate-siliciclastic margins and provides a useful
47 morphologic characterization and evolutionary model for assessing its tsunamigenic potential
48 with further numerical simulations. In addition, the discovery of a cold-water coral
49 community on top of the largest knoll has implications for identifying similar landslide-origin
50 cold-water coral communities on the GBR margin.

51

52 *Keywords:*

53 Continental slope; Slope failures; Mass transport deposits; Tsunamigenic potential; Cold-
54 water coral; Great Barrier Reef

55

56 **1. Introduction**

57 Late Pleistocene and Holocene sedimentary records and numerical modelling suggest that
58 submarine landslides have generated tsunami waves that might have reached significant
59 heights at the coast (Bondevik et al., 1997, 2005; Fisher et al., 2005; Geist et al., 2009; Özeren
60 et al., 2010; Iglesias et al., 2012). Landslide-generated tsunamis in recent times have created
61 noticeable material damage and loss of lives, for example the 1979 Nice tsunami (Antibes city
62 inundated, 8 fatalities; Assier-Rzadkiewicz et al., 2000; Sahal and Lemahieu, 2011), the 1998
63 Papua New Guinea tsunami (structures fully along the coast, over 2100 fatalities; McSaveney
64 et al., 2000; Synolakis et al., 2002), and the 1929 Grand Banks tsunami (12 telegraph cables,
65 28 casualties; Fine et al., 2005). Therefore, although most submarine landslides are not
66 tsunamigenic, their study has significant implications for assessing the potential natural
67 hazards facing populated coastal areas.

68 Submarine landslides occur in different tectonic settings with many of them reported
69 within the Quaternary. Glaciated margins host the largest landslides (10,000s km² and a few
70 1000s km³) on Earth (Laberg and Vorren, 2000; Haflidason et al., 2004; Vanneste et al.,
71 2006), together with those related to the collapse of the volcanic flanks from oceanic islands
72 (Moore et al., 1989; Masson et al., 2002). In contrast, landslides on active tectonic margins
73 are generally much smaller (10s to few 1000s km² and a few 10 km³; Tappin et al., 2001; von
74 Huene et al., 2004; Fisher et al., 2005; Harders et al., 2010; Strozyk et al., 2010) because the
75 higher frequency of seafloor shaking by earthquakes in those settings. Earthquakes are one of
76 the most important triggering mechanisms of slope failures (Locat and Lee, 2002; Masson et
77 al., 2002) and it is suggested that frequent large earthquakes might limit the landslide volume
78 on such active margins (Tappin et al., 2007; Völker et al., 2012). However, studies on
79 submarine mass-wasting are relatively scarce on modern carbonate or mixed carbonate-
80 siliciclastic passive margins (Hine et al., 2002; Puga-Bernabéu et al., 2013a; Principaud et al.,
81 2015; Tournadour et al., 2015; Webster et al., 2016). Given that one of the preconditioning
82 factors for landslide generation might be the presence of weak layers in the sedimentary
83 succession (Haflidason et al., 2003; Laberg et al., 2003; Harders et al., 2010), it is important
84 to note that the intrinsic characteristics of mixed carbonate-siliciclastic margins are the
85 variable lithologies with different rheologic properties which vary spatially and temporally.
86 Furthermore, recent studies have shown that submarine landslides might favour deep-water
87 coral bank development by creating a suitable substratum where cold-water corals can settle
88 on (De Mol et al., 2009; Savini et al., 2016).

89 In this study, we investigated the Great Barrier Reef (GBR) margin of north-eastern
90 Australia, the largest extant mixed carbonate-siliciclastic province in the world (Davies et al.,
91 1991a). Based initially on multibeam bathymetry along the GBR margin, we identified a large
92 km-scale (20 km wide and 8 km across) indentation in the margin and the associated blocks
93 and larger knolls found downslope at the toe of the slope, which are interpreted as a
94 submarine landslide complex, herein called the Gloria Knolls Slide (GKS). We present the
95 most comprehensive and high-resolution bathymetric and sub-bottom profile datasets
96 available for the region, and describe the main surface and subsurface geomorphologic
97 characteristics of the GKS. We then discuss the timing, possible pre-conditioning factors and
98 triggering mechanisms, and compare the results with landslides generated in other tectonic
99 settings. We also performed a simple first order estimation of the tsunamigenic potential of
100 the GKS which, together with its morphologic characterization, provides useful information
101 for more robust numerical simulations in the future aiming to assess the generation,

102 propagation and impact of potential tsunamis generated by the submarine landslides shaping
103 this margin.

104

105 **2. Regional setting**

106 The north-eastern Australia margin is a passive continental margin that constitutes a large
107 depositional area, from the shallow-water environment of the GBR shelf to the deeper slope
108 and basin settings in the adjacent Queensland Trough (Fig. 1). The study area is located on the
109 central part of this margin opposite the town of Innisfail. The shelf is a gently dipping surface,
110 about 65 km wide, with the shelf-break located at 102 to 109 m depth (Abbey et al., 2011).
111 The outer-shelf includes a series of submerged features, such as barrier reefs, lagoons,
112 pinnacles and terraces (Abbey et al., 2011; Hineostrova et al., 2016). The shelf is connected to
113 a moderately steep (4° to 7°) continental slope. Regionally, the slope is excavated by a
114 submarine canyon system perpendicular to the margin that extends to the base of the slope
115 between about 900 to 1200 m, and deepens towards the north (Puga-Bernabéu et al., 2013b;
116 Fig. 1A). The slope area studied in detail is located about 6 km south of Noggin Canyon 17
117 (Puga-Bernabéu et al., 2013b; Fig. 1B), and a potential landslide block called the “Noggin
118 Block” found perched at the head of this canyon (Puga-Bernabéu et al., 2013a). The
119 continental slope passes laterally to the basin floor of the Queensland Trough. The axis of this
120 trough gently deepens towards the north with an average gradient $<0.15^{\circ}$ (Puga-Bernabéu et
121 al., 2013b).

122 Modern surface sediments on the slope and in the basin comprise both terrigenous
123 siliciclastics and biogenic carbonates with a variable spatial distribution along the margin
124 (Dunbar et al., 2000; Francis et al., 2007). Subsurface slope sediments collected during ODP
125 Leg 133 (Sites 819, 820 and 821; Fig. 1A) about 70 km north of the study area, revealed the
126 presence of mixed carbonate-siliciclastic sediments since the Late Pleistocene at about 400 m
127 below the seafloor (Davies et al., 1991). These deposits comprise couplets of clay-rich and
128 carbonate-rich oozes that form fining upward, carbonate-decreasing sequences, and
129 coarsening upward, carbonate-increasing sequences. These sequences are disrupted by mass
130 movement deposits found throughout the cores (Davies et al., 1991a). In the deeper basin,
131 long sediment cores (ODP Leg 133 Site 823; Fig. 1A) reveal the presence of interbedded
132 hemipelagic muds, turbidites, debris flows and slump deposits since the Middle Miocene
133 (Watts et al., 1993). Closer to the study site, short cores (FR4/92 PC12, PC16; Fig. 1A) record
134 sediments varying between carbonate-rich and siliciclastic-rich intervals, and occasional thin
135 turbidite layers (Dunbar et al., 2000; Page et al., 2003).

136

137 **3. Material and methods**

138 3.1. Multibeam data

139 During a 2007 RV *Southern Surveyor* voyage (Webster et al., 2008), a group of large
140 knolls were located in the Queensland Trough, initially identified using GLORIA sidescan
141 imagery (Hughes-Clarke, 1994) and hence called the Gloria Knolls, which showed up as
142 clusters of high-reflectance pixels contrasting against a generally featureless area of the
143 trough. A Kongsberg EM300 multibeam system was used to survey an area of approximately
144 20 km x 20 km over the site in depths of about 1100 to 1300 m. All bathymetry data were
145 post-processed in Caris HIPS/SIPS software to remove any noise and adjust for sound
146 velocity in the water column. The cleaned ASCII xyz (long, lat, depth) records were imported
147 into ESRI raster grid files and QPS Fledermaus SD files as digital elevation models (DEMs)
148 using a grid pixel size of 30 m. Another RV *Southern Surveyor* voyage in 2008 (Tilbrook and
149 Matear, 2009) collected additional EM300 multibeam data along the GBR margin upslope of
150 the knolls site and across a large scarp found on the continental slope (Fig. 1). These
151 multibeam bathymetric datasets, plus all previously available bathymetry data for the GBR,
152 were compiled to produce both 30 and 100 m DEMs for the study area (Beaman, 2010).

153

154 3.2. GIS analysis

155 The geomorphometric analysis included the calculation of slope gradient, maximum slope
156 direction and surface curvature using ArcGIS Spatial Analyst tools on the 30 m and 100 m
157 DEMs. The slope gradient was calculated for each pixel based on the elevation of its nearest
158 neighbours in a 3 x 3 pixel window. Maximum slope direction (aspect) was classified into
159 eight groups of values corresponding to the cardinal points. Plan curvature was calculated
160 perpendicular to the direction of the maximum slope and allows the differentiation of ridges
161 (positive values) and valleys (negative values). Profile curvature was calculated in the
162 direction of the maximum slope, with positive values corresponding to upwardly concave
163 surfaces and negative values to upwardly convex surfaces.

164 To understand the potential volume loss of the material removed from the GBR margin due
165 to the GKS, a pre-slide continental slope 30 m DEM was developed in ArcGIS that followed
166 the general gradients of the non-scarp slope area found to the north and south of the larger
167 scarp feature. The ArcGIS Spatial Analyst Cut/Fill application was then used to calculate a
168 net loss of slope by comparing the volume loss of the reconstructed initial surface against the
169 observed scarp surface.

170

171 3.3 Sub-bottom profile data

172 During 2007 and 2008, a Kongsberg TOPAS PS-18 seismic system was used to acquire
173 shallow sub-bottom profiles from the outer-shelf, across the continental slope and into the
174 Queensland Trough. Several long transects were acquired over the Gloria Knolls themselves
175 in water depths of about 1200 to 1300 m. Two representative across and along sections over
176 the basin floor adjacent to the GKS headscarp and one section over the knolls site were
177 selected. The resulting SEG file profiles were viewed with the application DMNG SeiSee,
178 and representative gray-scale profiles were exported as bitmap images to manually draw
179 interpreted sub-bottom strata within Adobe Illustrator software. The Y axis units from the
180 profile were converted to depth in m, using TWT in ms and assuming a sound velocity of
181 1550 m s^{-1} (Davies et al., 1991a).

182

183 3.4. Rock dredge and sediment data

184 In 2007, a single rock dredge was taken across the crest of the largest knoll No. 1
185 ($17^{\circ}18.07'S$, $146^{\circ}56.10'E$) in a depth of about 1170 m (see Fig. 1B for location). The chain
186 mesh bag was full and contained about 1 m^3 of sediment, which was first sorted by hand to
187 remove any semilithified and lithified nodules, fossil material and live biota, and then
188 thoroughly washed through a 1 cm sieve to retain any smaller samples. All live biota were
189 preserved in ethanol, and the fossil samples were dried and then stored for post-cruise age
190 dating and taxonomic identification.

191 Sedimentological analyses were conducted on the components of the sediment matrix,
192 which included: (1) carbon, nitrogen and sulfur (CNS) weight percent, and CaCO_3 weight
193 percent on three representative samples of soft mud, a semi-lithified nodule and a lithified
194 nodule; (2) Wentworth size classes using a Malvern laser particle sizer for the mud fraction
195 ($<0.063 \text{ mm}$), sand fraction (0.063 to 2 mm) and gravel-fraction ($>2 \text{ mm}$) as volume percent
196 on two samples of soft mud and semi-lithified nodules (i.e. excluded lithified nodules).
197 Sediment was classified following Folk (1954); and (3) XRD analyses of the carbonate,
198 quartz and clay weight percent on three samples of soft mud, semi-lithified nodule and
199 lithified nodule. Additionally, two thin section slides were taken of the lithified nodules to
200 ascertain if they had an internal structure, such as concentric concretions or pellets.

201

202 3.5. Age data

203 Age dating for this study comes from 13 ages provided by accelerator mass spectrometry
204 (AMS) radiocarbon analysis of fossil samples conducted at the Australia Nuclear Science and
205 Technology Organisation (ANSTO). In addition, sub-samples of three fossil scleractinian
206 corals that were used for AMS dating were also analysed to provide three paired U-Th ages
207 (yr BP; see Supplementary Material 1 for U-Th dating methods). The radiocarbon ages were
208 calibrated using the Marine13 calibration curve (Reimer et al., 2013). It should be noted that
209 this calibration curve is for surface waters (to a depth of 75 m) and as these corals are from
210 deep waters, so these calibrations can only be approximations. Calibrations were performed
211 using a local reservoir age, ΔR , which was determined from the U/Th age (representing the
212 atmospheric ^{14}C age) and measured marine age from the same sample as described in detail
213 by Russell et al. 2011 (Equation 1). The modelled marine age was obtained interpolating the
214 measured atmospheric ^{14}C age against the Marine13 calibration curve. ΔR is then the
215 difference between the measured ^{14}C marine age and the modelled marine age. The error for
216 ΔR is calculated as shown in Equation 2 (Weisler et al. 2009).

217

$$218 \quad \Delta R = \text{measured marine age} - \text{modelled marine age} \quad (1)$$

$$219 \quad \sigma\Delta R = (\sigma \text{ measured age}^2 + \sigma \text{ modelled age}^2)^{0.5} \quad (2)$$

220

221 While three radiocarbon U-Th paired ages were determined, only one pair was suitable for
222 the local reservoir age determination. The paired dates for OZL547 were not used as the ages
223 are close to the ^{14}C background and the second pair of dates for OZL549 had a large error
224 associated with the U-Th age. The modelled marine reservoir age for OZL548 was estimated
225 by modelling in CALIB 7.1 (Stuiver et al. 2005) against the Marine13 curve, with $\Delta R = 0$.
226 The modelled value of 1510 ± 10 ^{14}C yrs BP gave a calibrated age range similar to the
227 atmospheric age range determined by the U-Th dating (Weisler et al. 2009). Thus the local
228 reservoir age was calculated from the paired U-Th age for OZL548 and gave a ΔR of
229 $1,045 \pm 75$ ^{14}C years BP.

230 This regional reservoir age was then used in the calibration of the radiocarbon ages, using
231 the Marine13 dataset within CALIB 7.1 (Stuiver et al., 2005), with the results shown in Table
232 4.

233

234 **4. Results**

235 4.1. Seafloor morphology and structure of the Gloria Knolls Slide complex

236 The GKS source area and deposits are located between ~75 to 100 km offshore the coastal
237 town of Innisfail, from 17°12.50'S to 17°25'S, and 146°41.75'E to 147°00'E (Fig. 1). The
238 GKS excavated a ~174 km² area of the GBR margin slope at water depths from 250 to 1080
239 m, with slide debris extending out to 1350 m depth. The horizontal dimensions of the source
240 area range from an along-slope distance of 20 km to about 8 km across-slope, forming a large
241 re-entrant indentation of the slope at this location, about 7 km seaward from the shelf-edge
242 and the reef-front (Figs. 1 and 2; Table 1A). Three main seafloor terrains can be distinguished
243 based on seafloor morphology.

244

245 *4.1.1. Source area and slide mass*

246 The source area is located on the slope below 250 m depth and is formed by a main slide
247 scar that marks the detachment of the upper slope, and a secondary scarp in deeper water
248 (Figs. 1 and 2). The main headwall scarp has a bow shape and a maximum height of 830 m.
249 The gradient in this scarp is much steeper (15-17° average) compared to the gradient of the
250 reconstructed initial slope and the non-failure slope area lying to the north and south of the
251 scarp (~6-7°; Fig. 3). The secondary scarp, similar in shape, is located in the southern part of
252 the GKS at ~670 m depth, with a height of 400 m and an average gradient of 17° (Figs. 1, 2
253 and 3). The toe of the scarps displays two parts with an arcuate morphology in plan-view
254 separated by a central area. This central area remained less affected after the slide, with
255 gentler slope gradients (~8°; Fig. 3, profile 3). No tensional cracks or pockmarks are observed
256 on the upper slope shoulder landward of the main headwall scarp. The source area is now
257 carved by small <1 km wide and <100 m deep gullies in the northern part of the main
258 headwall and a larger >2 km wide and >250 m deep, single canyon in the southern part (Fig.
259 1B). The gullies or canyons are oriented perpendicular to the direction of the main headwall
260 scar and do not cut into the shelf. Lying north and south of the scarp at the foot of the slope
261 are also small landslide scarps with cohesive debris zones lying close to the foot of the slope
262 (Figs. 1B and 2F; Puga-Bernabéu et al., 2013b).

263 The cut/fill analysis and the comparison between pre- and post-failure slope cross sections
264 yield a maximum thickness of the mass involved in the slide complex ranging from 260 to
265 500 m (south to north; Fig. 3), with an estimated net loss volume of 32 km³ of slope sediment
266 after the failure events.

267

268 *4.1.2. Proximal depositional area (PDA)*

269 The PDA extends over 10 to 14 km across the basin floor from the toe of the headwall
270 scarp at depths between 1050 and 1200 m (Fig. 2A). The seafloor is flat and smooth, with
271 gradients $<1^\circ$ both across and along the basin floor (Fig. 2B). No debris accumulation zone is
272 obvious directly adjacent to the base of this scarp, although part of the evacuated sediment
273 from the source area remains buried under hemipelagic sediment (see Section 4.2). The net
274 downslope direction visible in the aspect map is to the east-northeast (Fig. 2C). The planar
275 curvature map (Fig. 2D) shows subtle elongated, concave-up (negative curvature) features on
276 the seafloor but there is no clear evidence of linear features suggesting glide tracks (e.g.
277 Nissen et al., 1999).

278

279 *4.1.3. Distal depositional area (DDA)*

280 The DDA extends from about 1200 to 1350 m depth (Fig. 2A), and represents the main
281 observed depocentre of the GKS. The seafloor evolves from relatively flat in the PDA to an
282 uneven, hummocky surface in this area. Two depositional slide features are observed: large
283 blocks (i.e. the knolls); and smaller debris blocks (Figs. 2 and 4).

284 The distinctive cluster of eight knolls covers an area over the surrounding seafloor of ca.
285 15.3 km^2 with the shortest distance between two adjacent knolls of 300 m and the longest
286 distance of 3.4 km (Fig. 4; Table 2; Supplementary Material 2). The area of the largest knoll
287 (No. 1) is about 7.9 km^2 with a height above the surrounding seafloor of 105 m and is ~ 3.6
288 km long. The smallest knoll in size (No. 4) is approximately 0.5 km^2 in area with a height of
289 63 m and is 900 m long. The knolls range in height from 179 m (No. 5) to 44 m (No. 2) above
290 the surrounding seafloor. The knolls generally have rounded crests although several knolls
291 (Nos. 2, 4) show ridge-like crest morphology. Their perimeter shapes vary from near-elliptical
292 (Nos. 1, 3, 5) to more elongate shapes (Nos. 2, 4), with no obvious preferred orientation.
293 Some knolls have additional ridges extending from the crests and down their sides (Nos. 1, 5,
294 8). All knolls show evidence of moats on their northern sides which excavate between about
295 12 to 44 m into the adjacent surrounding seafloor (Fig. 4). The maximum runout distance
296 extends to about 30 km when measured from the top of the main headwall scarp to the
297 furthestmost knoll. This maximum runout distance could not be more accurately resolved by
298 measuring the displacement of the failed sediment mass centre (Lastras et al., 2004b), as
299 much of the sediment has subsequently been evacuated.

300 Also within the DDA, over 70 individual smaller debris blocks are distributed over an
301 uneven, topographically irregular seafloor around the eight larger knolls, displaying a pattern
302 of small elevated blocks separated by linear to sinuous depressions (Fig. 2E). The debris in

303 the northern part are nearly-circular, regularly spaced, small at 5 to 15 m high, and 300 to 500
304 m wide (Fig. 4). The gradients of the eastern side of the smaller debris blocks are steeper (3-
305 4°) than the western sides (<1°). Some of the smaller debris form arcuate ridges separated by
306 deeper depressions. In the southern part of the DDA, westwards from knoll No.1, debris are
307 larger and elongated in shape (Fig. 4).

308

309 4.2. Sub-bottom expression

310 The sub-bottom profiles across and along the basin floor over the GKS allowed us to
311 recognize different seismic reflection patterns in the proximal and distal depositional areas
312 identified on the seafloor bathymetry (Fig. 5).

313 At the toe of the slope, in the PDA, the uppermost strata form a relatively thin (~10 ms)
314 wedge-shaped body of chaotic to nearly transparent, low-amplitude reflectors occurring just
315 below the seafloor (Fig. 5A). This body shows small toe thrusts (Fig. 5A), and it corresponds
316 to a mass-transport deposit younger than those forming the GKS, which lies some metres
317 below. Seawards from this deposit, near-surface sediments consist of continuous parallel to
318 sub-parallel high amplitude reflectors bundled with low amplitude reflectors (Fig. 5B), which
319 correspond respectively to hemipelagic and sediment gravity flow (SGF) deposits. These
320 deposits represent the background sedimentation on this part of the basin (Dunbar et al., 2000;
321 Puga-Bernabéu et al., 2013a, 2014).

322 The internal character of the deeper deposits forming the GKS is different from the post-
323 failure strata described above. The mass-transport deposits in the GKS are identified below
324 the background drape as a partially confined, wedge-shaped bodies of mostly weak amplitude,
325 transparent reflectors in the PDA, and more discontinuous and chaotic in the DDA (Fig. 5A).
326 These bodies pinch out basinwards and laterally over about 20 km. In the PDA, some
327 continuous, high-amplitude sets of reflectors are intercalated between thick levels of
328 transparent reflectors (M1 and M2; Fig. 5B). A basal shear surface is not well observed in the
329 sub-bottom profiles but it presumably lies between 60 and 40 ms below the seafloor, forming
330 an irregular surface (Fig. 5B). The lateral boundaries of the slide are marked by onlap
331 terminations at the southern side and offset of the reflectors at the faulted northern side (Fig.
332 5B). Several blocks 300 to 400 m wide, characterized by nearly transparent reflection patterns
333 and rising from the adjacent reflectors, lie buried under the hemipelagic sediment drape in the
334 PDA (Fig. 5B). Towards the DDA, blocks of similar size crop out over the seafloor (Fig. 5A).
335 Within the DDA, discontinuous reflectors display imbricate or compressional patterns
336 forming small thrusts or pressure ridges at the toe of the slide (Fig. 5B). The total thickness of

337 the GKS deposits observed in the sub-bottom profiles parallel to the headwall ranges between
338 17 and 37 m (22 and 48 ms; Fig. 5B), with the thickest part in the southern half. In the
339 downslope direction, the thickness varies from 31 to 23 m (about 30 to 40 ms; Fig. 5A).

340 The sub-bottom profile over four of the larger knolls (Nos. 1, 3, 7, 8; Fig. 5C) also shows
341 other buried debris blocks, whose expression on the seafloor result in the uneven, irregular
342 topography between the knolls (Figs. 2 and 4). The profile shows up to 26 m below seafloor
343 of alternating strata, as opaque chaotic layers between parallel reflectors either side of the
344 knolls, which correspond to the background basin fill sediments. The knolls themselves are
345 relatively steep sided and the bulk of the blocks are acoustically opaque, but with up to 15 m
346 of less distinct strata capping the knolls (e.g. No. 1; Fig. 5C). Moats can also be seen as
347 notches in the seafloor on the northern sides of the knolls (Nos. 1, 3; Fig. 5C). The profile
348 therefore shows evidence that the slope failure occurred first, and over time the resulting
349 debris blocks were buried by alternating hemipelagic sediments and SGF deposits within the
350 basin.

351

352 4.3. Sediment description and dating results

353 4.3.1. Sedimentology

354 The dredge sample from knoll No. 1 recovered a matrix of stiff, light brown-coloured mud,
355 together with semi-lithified nodules and lithified nodules up to 15 cm in size. Many of the
356 nodules were covered in a Fe-Mn oxide crust (Supplementary Fig. 1). We investigated the
357 origin of the nodules to see if they were derived *in situ* from the soft mud sediment. The CNS
358 analysis of the soft mud, semi-lithified nodules, and lithified nodules resulted in low nitrogen
359 weights of 0.02 to 0.03%, and similar low sulphur weights of 0.03 to 0.04% (Table 3). There
360 were small but noticeable increases in the carbon weights from the soft mud (6.56%) to semi-
361 lithified (9.34%) to lithified nodules (10.55%), possibly due to an increasing proportion of
362 CaCO₃ cement as the nodules become lithified. The soft mud and semi-lithified nodules
363 showed mud fraction (<0.063 mm) volumes of 59.62% and 67.52% respectively, and sand
364 fraction (0.063 to 2 mm) volumes of 40.38% and 32.48% respectively. There were no gravel
365 fraction (>2 mm) volumes in these two samples. Both the soft mud and semi-lithified samples
366 are defined as a sandy mud. The XRD data indicate little variation in the bulk calcium
367 carbonate (78.1 to 83.5%), quartz (7.9 to 8.6%), and clay weights (7.8 to 13.6%) between the
368 three sample types. Interestingly, the XRD results of the mud fraction and sand fraction splits
369 from the soft mud and semi-lithified nodule reveal that the mud-sized components are
370 dominated by siliciclastics, and the sand-sized components are dominated by carbonates.

371 Therefore, the finer grains have likely been derived from land, whereas the sand is possibly
372 derived from hemipelagic/reefal carbonates. Additionally, the two thin sections taken from
373 the lithified nodules revealed no concentric concretions or the presence of pellets to their
374 internal structure.

375

376 4.3.2. Biota taxonomy

377 Interspersed within the sandy mud there was a remarkable variety of live and fossil biota
378 (Supplementary Fig. 1). Many fossil samples had Fe-Mn oxide sub-millimetre crusts on their
379 surfaces but there were also fossils that lacked any Fe-Mn staining. Samples of live biota
380 consisted of broken gorgonian seawhips (possibly *Nicella* spp. and *Viminella* spp.) up to 15
381 cm long, and broken unidentified scleractinian corals with their bases still attached to the
382 lithified nodules. Fossil samples were very common within the sediment matrix, and also
383 showed a preference for coral bases to be attached to lithified nodules. The colonial
384 scleractinian coral species identified were *Madrepora oculata*, *Enallopsammia rostrata*, and a
385 fossil species of *Enallopsammia* which could not be identified as an extant coral and is
386 possibly a new species (M. Kitahara personal communication). Solitary scleractinian corals
387 from the Family Caryophylliidae and numerous pieces of bamboo coral from the Family
388 Isididae were also found, either as disarticulated internodes or as broken branches up to 20 cm
389 in length. Small gastropods of a few cm in size whose assemblages of species (*Gemmula* sp.,
390 *Leucosyrinx* sp., *Pontiothauma* sp., *Calliotropis pagodiformis*) have previously been found in
391 about 1000 m of water off the North Island of New Zealand (B. Marshall personal
392 communication). Other molluscs included pteropods, bivalves and unidentified scaphopods.
393 Many loose plates of the stalked barnacle *Scillaelepas fosteri* were also scattered throughout
394 the sediment matrix. This barnacle species is previously recorded from the New Zealand sub-
395 Antarctic Islands (Newman, 1980), but this is the first record of that species from Australian
396 waters (D. Jones personal communication).

397

398 4.3.3. Ages

399 The rock dredge likely excavated only the top 0.5 m of the seabed surface of the knoll and
400 resulted in a random mixing of fossils (and therefore ages) for the individual samples. While
401 not as ideal as a long sediment core that would preserve the sequence of ages in the core, it
402 still provides a useful spread of ages to the fossil samples. The 13 uncalibrated ages range
403 from 2.28 ± 0.03 to 44.86 ± 0.85 kyr BP (Table 4). The calibrated ages range from 0.78 ± 0.14 to
404 greater than 50,000 cal kyr BP (the radiocarbon age exceeded the limit for the Marine13

405 calibration curve). The three samples with paired U-Th analyses have ages of:
406 301,899±19,105 (OZL547); 1,066±34 (OZL548); and 914±306 (OZL549) yr BP. The old age
407 (301,899±19,105 kyr BP) from the U-Th analysis suggests that the two oldest radiocarbon
408 ages of about 45 kyr BP, likely represent background ages older than about 50 kyr BP, and
409 are radiocarbon-dead. Interestingly, one of these older samples is possibly an undescribed
410 (non-extant) species of *Enallopsammia*, while the other is a lithified nodule. Taken together,
411 these data reveal a spread of ages ranging from at least 302 kyr BP till modern times.

412

413 **5. Discussion**

414 **5.1. Evolution of the slope failure**

415 The failed sediment slabs of the GKS were evacuated, transported and disintegrated
416 downslope forming a suite of relatively well-preserved blocks embedded within a loose
417 matrix over the seafloor (e.g. Laberg and Vorren, 2000; Canals et al., 2004; Hogan et al.,
418 2013; Figs. 4 and 5). In the case of the GKS, the relatively flat seafloor adjacent to the toe of
419 the scarp and the absence of coherent blocks, extensional ridges and/or other deformation
420 structures at this proximal location (Gardner et al., 1999; Lastras et al., 2006; Hogan et al.,
421 2013) point to a complete evacuation of the collapsed material. The presence of slope gullies
422 excavated into the headwall scarp and the lack of hanging terraces in the headwall area, also
423 support this fact. The available data suggest that sediment evacuation did not occur in a single
424 event but likely as a result of several events formed by retrogressive sliding. The presence of
425 a secondary scarp in the southern part of the GKS (Fig. 2) can be considered an evidence of
426 multi-phase instability (Canals et al., 2004; Twichell et al., 2009). Sub-bottom seismic
427 profiles show the presence of at least two chaotic mass-transport deposits separated by
428 hemipelagic sediments (Fig. 5B). Collapsed blocks, however, rise from deeper positions
429 within the sediment cover (Fig. 5A, B), and thus they were presumably emplaced before the
430 first mass-transport deposit shown in Figure 5B.

431 Based on the morphometric analysis of the bathymetry data combined with cross-sectional
432 sub-bottom profiles, we interpret that the present-day expression of the GKS resulted from a
433 sequential failure process spreading successively from the lower slope to the upper slope (Fig.
434 6). Under an external trigger mechanism (see Section 5.3), sediment destabilization initiated
435 at the lower slope, likely at water depths of the secondary headwall scarp, moved downslope
436 and disintegrated over the basin floor leaving some coherent debris (Event 1), some of which
437 were prominent enough to remain above the seafloor during subsequent burial phases (Fig. 5).
438 Sub-bottom profiles do not allow us to discern whether compressive structures formed at the

439 distal part of the landslide. Although variable, the orientation of the long axes of some large
440 blocks is perpendicular to the transport direction which may result from compression
441 (Huvenne et al., 2002). The removal of large amounts of sediments in this first stage could
442 therefore lead to an increase in slope angle, favouring subsequent slope instabilities. The
443 following collapse (Event 2) involved the emplacement of the first large mass-transport
444 deposit (M1 in Fig. 5B), which moved over the seafloor passing through the previous debris
445 and infilling the irregular surface left behind by the earlier event. Disintegrated material
446 reached the distal area and was locally subject to compression, likely due to the presence of
447 the hummocky surface, forming small thrusts or pressure ridges (Figs. 5A and 6). This second
448 event was followed by a period of hemipelagic deposition and intercalated SGF (debrites and
449 turbidites; Event 3) as shown in the sub-bottom profiles (Fig. 5B), suggesting that dismantling
450 of the slope did not stop completely. These later deposits were progressively smoothing the
451 seafloor surface. The third event is represented by another large mass-transport deposit (M2 in
452 Fig. 5B) which was emplaced similarly to the second event, including the formation of
453 pressure ridges. Although we cannot accurately determine this from available data, we
454 hypothesize the following links between the mass-transport deposits M1 and M2 of events 2
455 and 3 and their source areas. Due to the larger size of the mass-transport deposit M1
456 compared with M2 (Fig. 5B), the event 2 was linked to the formation of the main GKS scarp.
457 Additionally, event 3 might be related to a re-shaping of the remaining slope. Post-failure
458 hemipelagic sedimentation progressively buried the landslide deposits, and canyons and
459 gullies began at the failed slope. At more recent times, smaller landslides events, likely
460 related to canyon and gully activity, were deposited at the toe of the GKS scarp (Figs. 5A and
461 6).

462 While the inception and evolutionary model proposed for the GKS could be improved by
463 additional sub-bottom data, it is consistent with the morphologic features observed on the
464 adjacent seafloor to the south and north of the headwall. Here, the lower slope is dissected by
465 a more or less continuous set of smaller landslides whose scarps are located at similar depths
466 to that of the secondary GKS scarp (~670 m; Figs. 1B and 2). This may suggest that this part
467 of the slope is prone to collapse under specific triggering mechanisms. Furthermore, the upper
468 slope is affected by incipient sliding (Puga-Bernabéu et al., 2013a) which could be a smaller-
469 scale analogue of the second GKS event.

470

471 **5.2. Timing**

472 On passive margins such as north-eastern Australia, the timing of slope failures is thought
473 to be related to sea-level variations, especially during glacial times and transition to
474 interglacial periods (Owen et al., 2007; Lee, 2009; Webster et al., 2016). However, at the
475 global scale, there is no significant statistical correlation of landslide frequency with sea-level
476 changes (Urlaub et al., 2013). We have constrained the timing of the first GKS event by using
477 the radiometric age of fossil biota recovered from the surface of the largest slide block, which
478 provides a minimum age of emplacement. The oldest sample dated in this study (302 ± 19 kyr
479 BP, Table 4) are from a surface dredge, hence older material lying deeper within the sediment
480 were not sampled. However, the ~ 14 to 15 m of sediment strata capping the knolls provide an
481 additional constraint on the emplacement age. Two nearby sediment cores, FR4/92 PC12 and
482 FR4/92 PC16 (Fig. 1A) yielded overall sedimentation rates of 0.034 and 0.09 m kyr⁻¹ (derived
483 from age models based on correlation of sediment properties to SPECMAP; Dunbar et al.,
484 2000). The sedimentation rate on top of the knolls is likely to be lower due to their elevated
485 positions and the effect of increased current velocities. This effect can be seen in the
486 thickness of the sediment package covering knoll No. 7, which is approximately half as much
487 as the adjacent sediment from the surrounding seafloor (Fig. 5). The FR4/92 sediment cores
488 therefore provide a maximum constraint on the sedimentation rate on the knolls. For ~ 14 to
489 15 m to accumulate at a rate of 0.034 m kyr⁻¹, the knolls must have been in place for likely
490 412 to 441 kyr BP. Taken together, these constraints suggest the emplacement of the large
491 knolls (event 1) likely occurred during the transition from Marine Isotopic Stage 12 to 11,
492 when the amplitude of the sea-level change was the largest in the last million years (Lisiecki
493 and Raymo, 2005; Rohling et al., 2014). The timing for the subsequent younger slide events
494 (see Section 5.1) cannot be assessed with the available data.

495

496 **5.3. Triggering mechanisms and pre-conditioning factors.**

497 The triggering mechanisms for submarine landslides include different processes which
498 may act together to reduce the shear strength and lead to sediment mass failure downslope.
499 The most important triggers include high sedimentation rates and overpressure, ocean waves,
500 gas hydrate dissociation and seismic activity (Bea et al., 1983; Piper et al., 1999; Matsumoto
501 et al., 2003; Sultan et al., 2003, 2004a; Lafuerza et al., 2012; Crutchley et al., 2016).

502 High sedimentation rates may trigger slope failures by creating high excess pore pressures
503 in the sediment and/or by oversteepening (Baraza et al., 1990; Wolinsky and Pratson, 2007;
504 Dugan and Sheahan, 2012). These high rates are related to environmental factors such as sea-
505 level change and sediment input. It is widely accepted that during sea-level lowstands, large

506 amounts of terrigenous sediments are transported to the deep ocean basins which could favour
507 rapid sediment deposition (Posamentier and Vail, 1998; Posamentier and Erksin, 1991;
508 Carvajal and Steel, 2006; Normark et al., 2006). However, this is not the case for the GBR
509 margin, where the maximum rates of sediment supply to the slopes occurred during the late
510 transgression (Dunbar et al., 2000; Page et al., 2003). In the central GBR, many upper slope
511 landslides have been identified nearby a large deltaic system (paleo-Burdekin River lying
512 ~150 km to the south-east; Webster et al., 2016). However, the GKS study area lacks any
513 large deltaic or fluvial systems similar to the paleo-Burdekin River that may provide large
514 amounts of sediment to the slope. Sedimentation rates on the GBR uppermost slope, between
515 200 and 300 m depth, are relatively low to moderate, from 20 to 50 cm ky⁻¹ (Dunbar et al.,
516 2000). Therefore, it seems unlikely that high sedimentation rates alone can account for the
517 inception of the GKS.

518 Ocean waves, such as storm waves and tsunamis can generate cyclically oscillating high-
519 and low-pressure on the seafloor sediments, and in some cases have the potential to generate
520 slope failures (Sterling and Strohbeck, 1975; Bea et al., 1983; Rogers and Goodbred Jr., 2010;
521 Casalbore et al., 2012). The GBR margin is affected periodically by tropical cyclones
522 (Puotinen, 2004), and some of them pass right across the study area as in the case of the
523 Cyclone Yasi (Category 5) on the 3rd of February 2011 (Great Barrier Reef Marine Park
524 Authority, 2011; Perry et al., 2014). However, both the secondary and the main headwall
525 scarps of the GKS lies too deep (between 250 and 670 m depth) to be affected by direct
526 cyclone pumping even during sea-level low-stands.

527 Gas hydrate dissociation may influence the static stable sediment conditions on the slope
528 and lead to slope failures by modifying the sediment strength (Carpenter, 1981; Kayen and
529 Lee, 1991; Sultan et al., 2004c). Theoretically, gas hydrates may form at the depth of the
530 secondary headwall scarp of the GKS (670 m) and the gas hydrate stable zone may extend
531 about 100 m below the seafloor (based on Kvenvolden, 1988 and Ruppel, 2007). However, no
532 definitive gas hydrates have so far been identified in Australian waters (Geoscience Australia
533 and BREE, 2012). The contribution of gas hydrate dissociation to slope failure in the study
534 area cannot be evaluated with the available information, but its impact as a trigger cannot be
535 dismissed and requires further research.

536 Earthquakes are one of the most effective external processes for triggering slope failures
537 (Tappin et al., 2001; Fine et al., 2005). Although the GBR margin is a passive margin, recent
538 seismic events of small magnitude (mostly M_w 2-4, up to M_w 5) have occurred within a radius
539 of 150 km around the GKS location (Earth Systems Science Computational Centre, 2015;

540 Geoscience Australia, 2015). Slope stability simulations show that the margin slope in nearby
541 (<10 km) areas is stable under current static gravitational loading, but it may collapse under a
542 seismic event yielding a peak horizontal acceleration of 0.2-0.4 g (Puga-Bernabéu et al.,
543 2013a). This horizontal acceleration can be generated at short hypocentral distances and short
544 periods by large M_w 7.0 earthquakes, which is consistent with the maximum earthquake
545 magnitude estimated elsewhere in Australia (MW 7. 0-7.5±0.2, Allen et al. 2011). The
546 seismic events might have a local source associated with the N-NW regional faults that affect
547 the basement and overlying sediments nearby the study area (Symonds et al., 1983).
548 Therefore, a unusually large seismic event could have acted as possible triggering mechanism
549 for the first event of the GKS.

550 Earthquake shaking, although an important trigger, probably represents the final push for
551 landslide generation, and thus pre-conditioning or susceptibility factors have also to be taken
552 into account. The presence of weak layers in the slope sedimentary successions favour slope
553 instabilities, as these beds can show different mechanical behaviour compared with the
554 surrounding sediment (Haflidason et al., 2003; Kvalstad et al., 2005). Weak layers can form
555 continuous horizons that may act as the slip plane for several slope failures. For example, in
556 the Eivissa Channel (western Mediterranean), the contact between hydro-mechanical
557 properties at the boundary between fine-grained sediments overlying methane-charge,
558 relatively coarse deposits acted as a failure surface for at least four slides (the Ana, Joan,
559 Nuna and Jersi slides; Lastras et al., 2004b, 2006; Lafuerza et al., 2012). In the GKS study
560 area, no long sediment cores are directly available to assess the presence of weak layers.
561 However, seismic lines and long cores from the Ocean Drilling Program Leg 133 across a
562 slope transect (~70 km north of GKS, sites 819 through 821; Fig. 1A), provide useful
563 information about the sub-bottom stratigraphy of the margin. Sediments from these cores
564 record abundant Late Pleistocene multimetre-scale, coarsening-upward cycles with varying
565 proportions of carbonates and siliciclastics, from clay-rich sediments with numerous silt
566 intercalations to carbonate-rich bioclastic wackestones (Glenn et al., 1993). Interestingly, the
567 presence of a slump appears with strong amplitude mounded reflectors at the top of the
568 progradational seismic sequence 6 in site 819 (Davies et al., 1991b). The detachment surface
569 of this slump occurred at the top of one of the coarsening upward cycles, and the depth below
570 seafloor (~200 mbsf; Davies et al., 1991b) is similar to the depth of the secondary headwall
571 scarp of the GKS below the reconstructed pre-failure seafloor (profiles 4 and 5 in Fig. 3). We
572 suggest that the presence of alternating carbonate and siliciclastic lithologies, deposited
573 during successive sea-level cycles at different sedimentation rates on this mixed margin,

574 might have generated weak layers within the sediment package. Rapid sea-level changes, such
575 as during the MIS 12 to 11 transition when the first event of the GKS likely occurred, may
576 have also contributed to the slope failure due to rapid sediment building during deglacial
577 periods and transient excess pore pressures (Owen et al., 2007; Smith et al., 2013). Future
578 research could focus on obtaining long sediment cores and subsurface geophysical
579 information to better understand the pre-conditioning factors for mass-transport deposits in
580 this archetypical mixed carbonate-siliciclastic margin.

581

582 **5.4. Comparison with other submarine landslides**

583 The GKS is the largest landslide complex discovered so far on the north-eastern Australia
584 margin (Puga-Bernabéu et al., 2016), but as detailed knowledge of other slope failures is
585 virtually lacking on modern mixed carbonate-siliciclastic margins, we must compare this slide
586 against other settings. In terms of sediment composition, the most direct comparison is with
587 slope failures on the carbonate slopes of the Great Bahama Bank (GBB), the Little Bahama
588 Bank (LBB) and the Exmouth Plateau of north-western Australia (Scarselli et al., 2013; Jo et
589 al., 2015; Tournadour et al., 2015; Principaud et al., 2015). Large landslides on these margins
590 are similar in terms of size and morphology to the GKS. These landslides have semicircular to
591 box shapes, range from 10 to 23 km in length, 5 to 12 km in width, and remobilized about 15
592 to 30 km³ of eroded slope sediments. The maximum size of collapsed coherent blocks
593 remaining on the seafloor is also similar (about 2 km long). However, runout distances are
594 variable, from very short (1.2 km) to about 20 km (Jo et al., 2015; Principaud et al., 2015)
595 similar to the GKS. A significant difference with the GKS is the local development of slope
596 fan systems fed by channelized flows linked to slumps in the Exmouth Plateau (Scarselli et
597 al., 2013). The similar dimensions and characteristics of these landslides and the GKS might
598 indicate comparable physical properties of sediment in the pre-failed slope and initiation
599 processes. Landslide triggering mechanisms along the GBB and LBB margins include
600 tectonic activity and high sedimentation rates, while seismic loading and fluid venting are the
601 likely triggers along the Exmouth Plateau. However, as in the case of the GKS, these triggers
602 remain unproven and need further constraint.

603 On passive siliciclastic margins, submarine landslides are generally more numerous and
604 cover larger areas on the seafloor where the margin has been supplied by large river systems
605 or glaciers (Twichell et al., 2009). The GKS is not a large landslide compared with the giant
606 slope failures found in glaciated (or formerly) passive margins such as the Storegga Slide
607 (Haflidason et al., 2004), the Hinlopen Slide (Vanneste et al., 2006) or the Trænadjupet Slide

608 (Laberg and Vorren, 2000), although it is comparable in size to some large landslides in river-
609 fed passive margins (Canals et al., 2004; Lastras et al., 2002, 2004a; Ramprasad et al., 2011).
610 High sedimentation rates, which are able to generate excess pore pressure in the sediment,
611 likely influence the distribution of landslides in these margin types, particularly in the case of
612 glacially-influenced slopes (Laberg and Vorren, 2000; Solheim et al., 2005). On the north-
613 eastern Australia margin, sedimentation rates are low (see Section 5.3), and the controls and
614 timing on sedimentation rates differ from those in passive siliciclastic margins (Dunbar et al.,
615 2000; Dunbar and Dickens, 2003; Page et al., 2003) where they are driven by climate change
616 between glacial and interglacial conditions. Equally important seems to be the presence of
617 weak layers within the sedimentary succession, which are commonly linked to contourite
618 layers intercalated within hemipelagic deposits in the case of glaciated margins (Solheim et
619 al., 2005), or shelf-edge delta deposits and related bedding planes in the case of river-
620 influenced margins (Prior et al., 1986). However, the possible interaction between landslides
621 and contour currents (e.g. Krastel et al., 2011) remains uncertain in the GKS study area. As in
622 most cases on passive margin slopes, the GKS is interpreted to be formed as a retrogressive
623 slope failure, although the failed material is now fully evacuated. Passive margins far from the
624 influence of continental glaciers, including the north-eastern Australia margin, are overall
625 stable under present-day normal gravitational conditions (Baraza et al., 1990; Sultan et al.,
626 2004b; Urgeles et al., 2006; Puga-Bernabéu et al., 2013a), and thus landslide initiation usually
627 requires an external trigger, like a large earthquake.

628 The physiographic setting (shelf, slope, relatively shallow base-of-slope and basin), the
629 dimensions (e.g. headwall scar length, volume of remobilized sediment) and the
630 characteristics of the landslide areas defined for the GKS (source area, PDA and DDA) are
631 similar to the latest Pleistocene BIG'95 slide (debris flow) in the western Mediterranean
632 (Lastras et al., 2002, 2004a). Therefore, the comparison of similar seafloor expression,
633 kinematic indicators and sedimentary features distributed along the different landslides
634 domains (e.g. BIG'95 debris flow) may help to identify common patterns in the sediment
635 failure process. The BIG'95 debris flow was the result of several processes involving
636 materials with contrasting rheologies and specific source areas that led to deposition of a suite
637 of cohesive blocks in an intermediate depositional area and a debrite, formed by more mobile
638 material, in a distal depositional area up to 110 km far from the source area (Lastras et al.,
639 2002, 2004a). Numerical simulations suggest that the highly mobile sediment mass pushed,
640 sheared and accelerated in its movement downslope slabs of coherent sediments and
641 continued flowing downslope once the block eventually stopped, although the effect

642 hydroplaning cannot be discarded (Lastras et al., 2005). The knolls and debris distribution in
 643 the DDA of the GKS is comparable to that of the blocks and block clusters in the BIG'95
 644 debris flow, as well as the runout distance for such blocks (15-25 km). In contrast, apart from
 645 the disintegrated sediment surrounding the blocks, we have not identified slide sediments
 646 deposited out of the DDA in the GKS. We cannot discard the presence of such deposits as
 647 they might have been transported further downslope, now lying buried within the Queensland
 648 Trough (Fig. 1A), which may represent an analogue of the Valencia Channel in the case of the
 649 BIG'95 debris flow (Lastras et al., 2002, 2004a).

650

651 **5.5. Tsunamigenic potential**

652 The GKS is a relatively modest in size submarine landslide complex (Canals et al., 2004;
 653 Hühnerbach et al., 2004) but its dimensions, extending over 528 km² on the seafloor and
 654 remobilizing about 32 km³ of sediment, is large enough to be considered as a potential
 655 tsunamigenic landslide, as has been suggested for landslides of similar size (McAdoo et al.,
 656 2000; ten Brink et al., 2006; Iglesias et al., 2012). The speed of the slide mass represents a
 657 key requirement in the assessment of tsunami potential and the height of the resulting tsunami
 658 wave can be only estimated on the basis of numerical hydrodynamic modelling of each
 659 particular landslide (Todorovska et al., 2002; Trifunac et al., 2002; Puzrin et al., 2010).
 660 Although, the detailed 3D numerical modelling of the potential tsunami linked to the GKS is
 661 out of the scope of the present study, a simple, first order approach is possible if we consider
 662 the basic morphometric parameters quantified here. Assuming the simplest case, a
 663 translational slide with no basal friction and strong fluid dynamic drag (Grill et al., 2009 and
 664 references therein), the maximum three-dimensional tsunami amplitude (η_o) is given by:

$$665 \eta_o = S_o (0.0574 - 0.0431 \sin \theta) \left(\frac{T}{b}\right) \left(\frac{b \sin \theta}{d}\right)^{1.25} (1 - e^{-2.2(s-1)}) \left(\frac{w}{w + \lambda_o}\right) \quad (1)$$

666 where S_o is the distance of motion for translational failures,

$$667 S_o = \frac{\pi}{2} b(s + 1) \quad (2)$$

669 θ is the angle of the slope, T is the maximum thickness of the failed mass, b is the length of
 670 the slide mass, d the average depth above the center of the slide mass, s is the sediment
 671 specific gravity, w the slide mass width, and λ the tsunami wavelength,
 672

$$673 \lambda_o = \sqrt{\frac{\pi b d (s+1)^2}{2 s \sin \theta (s-1)}} \quad (3)$$

675
676 These numerical equations are valid within a range of $\theta \in [5, 30^\circ]$, $d/b \in [0.06, 1.5]$, T/b
677 $\in [0.008, 0.2]$, and $s \in [1.46, 2.93]$ which are satisfied by the morphometric values calculated
678 for the GKS.

679 The most conservative scenario is to consider a first large margin collapse at the depth of
680 the secondary headwall scarp (Fig. 2), corresponding to the first event (Fig. 6). According to
681 the predictive equations above, the sudden mass failure of this portion of the margin would
682 yield a three-dimensional tsunami wave elevation of about 27 m. These waves are about three
683 times greater than those modelled for the potential collapse of a small block (“Noggin Block”
684 $\sim 0.86 \text{ km}^3$) found on the upper slope 6 km north from the GKS (Puga-Bernabéu et al., 2013a).
685 Run-up heights at the adjacent coast would depend on the sea-level position, the overall
686 physiography of the margin, the period, size and direction of the incoming waves, beach
687 morphology, bottom friction, and other parameters. It has also been suggested that the
688 presence of the shelf reefs, if in existence at the time (Webster and Davies, 2003), would
689 decrease tsunami amplitudes at the coastline to half or less (Baba et al., 2007; Webster et al.,
690 2016). For example, the impact of a modelled 2 m high tsunami wave generated by a small-
691 scale landslide ($\sim 0.025 \text{ km}^3$) in the southern central GBR, would have reached the coast with
692 a height of 0.5 m (Webster et al., 2016). Nonetheless, a tsunami caused by the collapse of
693 GKS would have been significant even if dampened by shelf reefs. This simple approach
694 highlights the potential tsunami hazard of submarine landslides to the north-eastern Australia
695 coast and thus the need for better characterization of slope failure processes on this margin.

696

697 **5.6. Discovery of cold-water coral community**

698 The discovery of a variety of both live and abundant fossil biota from the top of one knoll
699 points to a cold-water coral community existing since at least 302 ka to modern times (Table
700 4 and Supplementary Fig. 1). The presence of three extant scleractinian coral species (and
701 possibly one undescribed non-extant species), to bamboo corals, gorgonians, stalked
702 barnacles, and various molluscs highlights a habitat that supports a cold-water coral
703 community. The knolls appear to meet the geomorphic and environmental requirements for
704 cold-water corals to settle and grow: (1) a suitable substratum of semi-lithified and lithified
705 nodules as the necessary hard surface to attach to by providing a stable anchorage in a
706 dynamic environment; and (2) food availability through locally accelerated currents over the
707 knolls (De Mol et al., 2009). The eight knolls, up to 179 m in height above the surrounding
708 seafloor, are likely to locally accelerate currents for enhanced food supply. Further, the moat

709 features on the northern sides of the knolls provide evidence for north-flowing currents
710 sweeping over the knolls, thereby scouring any sediment on the leeward side bases. Such
711 accelerated currents would also help to reduce sedimentation on the uppermost knoll surfaces
712 where cold-water corals may grow, another requirement for the presence of corals (De Mol et
713 al., 2009). The water mass at this depth is indicative of Antarctic Intermediate Water (AAIW;
714 Solokov and Rintoul, 2000; Hartin et al., 2011) found below 700 to 1000 m. AAIW enter the
715 Queensland Trough from the south and flows northwards towards the Coral Sea Basin
716 (Solokov and Rintoul 2000) and is likely responsible for the scouring of moats around the
717 knolls.

718 The existence of a cold-water coral community in the Queensland Trough provides a
719 further example of the spatial relationship existing between submarine landslides and the
720 presence of cold-water corals in the deep-sea (Viana et al., 1998; Huvenne et al., 2003; De
721 Mol et al., 2009; Correa et al., 2011, Savini et al., 2016). Elsewhere along the GBR margin in
722 depths to ~2000 m, we have identified smaller clusters of knolls, some up to 50 m high, near
723 other landslide features derived from the lower slope (Puga-Bernabéu et al., 2011). It would
724 be important to confirm if other blocks also have cold-water corals, as their environmental
725 conditions are similar. Indeed, the depth of collection at the Gloria Knolls (1170 m) for the
726 colonial scleractinia *Madrepora oculata* and *Enallopsammia rostrata*, conform to the depth
727 ranges of these same species previously sampled off Queensland in the Coral Sea (Cairns,
728 2004). These species lie within a tropical province of azooxanthellate scleractinian corals that
729 forms a subcluster of faunas with similarities to the Indo-Pacific seamounts and New Zealand
730 (Cairns, 2004). This current work, and future research, will provide important baseline
731 information for marine managers to assess the deep Great Barrier Reef and Coral Sea
732 biodiversity in relation to seabed topography and oceanographic processes.

733

734 **6. Conclusions**

735 The GKS is the largest submarine landslide complex discovered so far on the Great Barrier
736 Reef margin of north-eastern Australia. This slope failure removed 174 km² and remobilized
737 about 32 km³ of slope sediments during three mass-wasting events, leaving a steep headwall
738 scarp up to 830 m in height, now shaped by younger gullies and a canyon. The dimensions of
739 the GKS are within the range of submarine landslides in river-fed passive margins and
740 carbonate-dominated margins.

741 The main depocentre of the GKS is located in the distal part of the slide, where a
742 distinctive cluster of km-scale knolls and over 70 smaller debris blocks extend over an

743 irregular seafloor surface. The GKS deposits show weak amplitude, transparent reflectors in
744 the proximal depositional area and more discontinuous and chaotic in the distal depositional
745 area. In contrast, post-failure strata consist of continuous parallel to sub-parallel high
746 amplitude reflectors bundled with low amplitude reflectors.

747 The present-day expression of the GKS resulted from a sequential failure process
748 spreading successively from the lower slope to the upper slope. The GKS initiation was
749 probably the result of several processes involving varying carbonate and siliciclastic
750 lithologies in the region, favoured by a rapid relative sea-level rise, and most likely triggered
751 by an unusually large seismic event. The cold-water coral community identified on one of the
752 knolls provides important baseline information for marine managers to assess deep Great
753 Barrier Reef and Coral Sea biodiversity.

754

755

756 **Acknowledgments**

757 We thank the Captains and crew of the RV *Southern Surveyor* for their assistance during the
758 SS072007 and SS092008 expeditions, and the support of the staff at Australia's Marine
759 National Facility (<http://www.marine.csiro.au/nationalfacility/>). The 2007 voyage was also
760 funded by the National Geographic Society and the European Consortium for Ocean Research
761 Drilling. We thank Raphael Wust for the sediment analyses. The authors would like to thank
762 the Australian Research Council (DP1094001) for support and the Australia Institute of
763 Nuclear Science and Engineering for financial assistance (Award No. AINGRA09006) to
764 enable the AMS work on the fossil samples to be conducted. APB was also funded by the
765 Research Group RNM-190 of the Junta de Andalucía (Spain). We also thank two anonymous
766 reviewers for their constructive reviews.

767

768 **References**

769 Abbey, E., Webster, J.M., Beaman, R.J., 2011. Geomorphology of submerged reefs on the
770 shelf edge of the Great Barrier Reef: The influence of oscillating Pleistocene sea-levels.
771 *Marine Geology* 288, 61–78.

772 Allen, T.I., Burdidge, D.R., Clark, D., McPherson, A.A., Collins, C.D.N., Leonard, M., 2011.
773 Development of the next generation Australian National Earthquake Hazard Map. In:
774 Proceedings of the ninth Pacific conference on earthquake engineering, building and
775 earthquake-resilient society, Auckland, New Zealand, paper 207, p. 8.

- 776 Assier-Rzadkiewicz, S., Heinrich, P., Sabatier, P.C., Savoye, B., Bourillet, J.F., 2000.
777 Numerical modeling of a landslide-generated tsunami: The 1979 Nice event. *Pure and*
778 *Applied Geophysics* 157, 1707–1727.
- 779 Baba, T., Mleczko, R., Burbidge, D., Cummins, P., Thio, H.K., 2007. The Effect of the Great
780 Barrier Reef on the Propagation of the 2007 Solomon Islands Tsunami Recorded in
781 Northeastern Australia. *Pure and Applied Geophysics* 165, 2003–2018.
- 782 Baraza, J., Lee, H.J., Kayen, R.E., Hampton, M.A., 1990. Geotechnical characteristics and
783 slope stability on the Ebro margin, western Mediterranean. *Marine Geology* 90, 379–393.
- 784 Bea, R.G., Wright, S.G., Sircar, P., Niedoroda, A.W., 1983. Wave-induced slides in South
785 Pass Block 70, Mississippi Delta. *Journal of Geotechnical Engineering* 109, 619–644.
- 786 Beaman, R.J., 2010. 3DGBR. A high-resolution depth model for the Great Barrier Reef and
787 Coral Sea. Marine and Tropical Sciences Research Facility (MTSRF) Project 2.5i.1a Final
788 Report. MTSRF (12 pp. Data available at: [http://www.deepreef.org/bathymetry/65-3dgbr-](http://www.deepreef.org/bathymetry/65-3dgbr-bathy.html)
789 [bathy.html](http://www.deepreef.org/bathymetry/65-3dgbr-bathy.html)).
- 790 Bondevik, S., Svendsen, J.I., Mangerud, J. 1997. Tsunami sedimentary facies deposited by the
791 Storegga tsunami in shallow marine basins and coastal lakes, western Norway.
792 *Sedimentology* 44, 1115–1131.
- 793 Bondevik, S., Lovholt, F., Harbitz, C.B., Mangerud, J., Dawson, A.G., Svendsen, J.I. 2005
794 The Storegga slide tsunami—comparing field observations with numerical simulations.
795 *Marine and Petroleum Geology* 22, 195–208. Cairns, S.D., 2004. The Azooxanthellate
796 Scleractinia (Coelenterata: Anthozoa) of Australia. *Records of the Australian Museum* 56,
797 259–329.
- 798 Canals, M., Lastras, G., Urgeles, R., Casamor, J.L., Mienert, J., Cattaneo, A., De Batist, M.,
799 Haflidason, H., Imbo, Y., Laberg, J.S., Locat, J., Long, D., Longva, O., Masson, D.G.,
800 Sultan, N., Trincardi, F., Bryn, P., 2004. Slope failure dynamics and impacts from seafloor
801 and shallow sub-seafloor geophysical data: case studies from the COSTA project. *Marine*
802 *Geology* 213, 9–72.
- 803 Carpenter, G., 1981. Coincident sediment slump/clathrate complexes on the U.S. Atlantic
804 continental slope. *Geo-Marine Letters* 1, 29–32.
- 805 Carvajal, R., Steel, R.J., 2006. Thick turbidite successions from supply-dominated shelves
806 during sea-level highstand. *Geology* 34, 665–668.
- 807 Casalbore, D., Bosman, A., Chiocci, F.L., 2012. Study of Recent Small-Scale Landslides in
808 Geologically Active Marine Areas Through Repeated Multibeam Surveys: Examples from
809 the Southern Italy. In: Yamada, T., Kawamura, K., Ikehara, K., Ogawa, Y., Urgeles, R.,
810 Mosher, D., Chaytor, J., Strasser (Eds.), *Submarine mass movements and their*
811 *consequences*, 5th International Symposium, pp. 573–582.

- 812 Correa, T.B.S., Grasmueck, M., Eberli, G.P., Reed, J.K., Verwer, K., Purkis, S., 2011.
813 Variability of cold-water coral mounds in a high sediment input and tidal current regime,
814 Straits of Florida. *Sedimentology* 59, 1278–1304.
- 815 Crutchley, G., Mountjoy, J.J., Pecher, I.A., Gorman, A.R., Henrys, S.A., 2016. with Shallow
816 Gas Hydrate Systems: Insights from New Zealand Examples. In: Lamarche, G., Mountjoy,
817 J., Bull, S., Hubble, T., Krastel, S., Lane, E., Micallef, A., Moscardelli, L., Mueller, C.,
818 Pecher, I., Woelz, S. (Eds.), *Submarine mass movements and their consequences*,
819 *Advances in Natural and Technological Hazards Research* 41, 401–410.
- 820 Davies, P.J., McKenzie, J.A., Palmer-Julson, A., et al., 1991a. *Proceedings of the Ocean*
821 *Drilling Program Initial Reports 133*. Ocean Drilling Program, College Station, TX.
- 822 Davies, P.J., McKenzie, J.A., Palmer-Julson, A., et al., 1991b. *Proceedings of the Ocean*
823 *Drilling Program Initial Reports 133, Site 819*. Ocean Drilling Program, College Station,
824 TX, pp. 451–508.
- 825 De Mol, B., Van Rensbergen, P., Pillen, S., Van Herreweghe, K., Van Rooij, D., McDonnell,
826 A., Huvenne, V., Ivanov, M., Swennen, R., Henriot, J.P., 2002. Large deep-water coral
827 banks in the Porcupine Basin, southwest of Ireland. *Marine Geology* 188, 193–231.
- 828 De Mol, B., Huvenne, V., Canals, M., 2009. Cold-water coral banks and submarine
829 landslides: a review. *International Journal of Earth Sciences* 98, 885–899.
- 830 Dugan, B., T.C. Sheahan. 2012. Offshore sediment overpressures of passive margins:
831 Mechanisms, measurement, and models. *Reviews of Geophysics* 50, RG3001,
832 <http://dx.doi.org/10.1029/2011RG000379>.
- 833 Dunbar, G.B., Dickens, G.R., 2003. Massive siliciclastic discharge to slopes of the Great
834 Barrier Reef Platform during sea-level transgression: constraints from sediment cores
835 between 15°S and 16°S latitude and possible explanations. *Sedimentary Geology* 162, 141–
836 158.
- 837 Dunbar, G.B., Dickens, G.R., Carter, R.M., 2000. Sediment flux across the Great Barrier Reef
838 Shelf to the Queensland Trough over the last 300 ky. *Sedimentary Geology* 133, 49–92.
- 839 Earth Systems Science Computational Centre (2011) University of Queensland. Queensland
840 earthquake map, Cairns region. <http://www.quakes.uq.edu.au>. Accessed 15 July 2015.
- 841 Fine, I.V., Rabinovich, A.B., Borhold, B.D., Thomson, R.E., Kulikov, E.A., 2005. The
842 Grand Banks landslide-generated tsunami of November 18, 1929: preliminary analysis and
843 numerical modeling. *Marine Geology* 215, 45–57.
- 844 Fisher, M.A., Normark, W.R., Greene, H.G., Lee, H.L., Sliter, R.W., 2005. Geology and
845 tsunamigenic potential of submarine landslides in Santa Barbara Channel, Southern
846 California. *Marine Geology* 224, 1–22.

- 847 Folk, R.T., 1954. The distinction between grain size and mineral composition in sedimentary-
848 rock nomenclature. *Journal of Geology* 62, 334–359.
- 849 Francis, J.M., Dunbar, G.B., Dickens, G.R., Sutherland, I.A., Droxler, A.W., 2007.
850 Siliciclastic sediment across the North Queensland margin (Australia): A Holocene
851 perspective on reciprocal versus coeval deposition in tropical mixed siliciclastic-carbonate
852 systems. *Journal of Sedimentary Research* 77, 572–586.
- 853 Gardner, J.V., Prior, D., B., Field, M.E., 1999. Humboldt Slide - a large shear-dominated
854 retrogressive slope failure. *Marine Geology* 154, 323–338.
- 855 Geoscience Australia, BREE, 2012. Australian Gas Resource Assessment 2012, Canberra, 68
856 p.
- 857 Geoscience Australia (2012) Earthquake Database.
858 <http://www.ga.gov.au/earthquakes/searchQuake.do>; accessed December 2016.
- 859 Glenn, C.R., Kroon, D., Wei, W., 1993. Sedimentary rhythms and climatic forcing of
860 Pleistocene-Holocene mixed carbonate/siliciclastic sediments off the Great Barrier Reef.
861 In: McKenzie, J.A., Davies, P.J., Palmer-Julson, A., et al., 1993. Proceedings of the Ocean
862 Drilling Program Scientific Results 133. Ocean Drilling Program, College Station, TX., pp.
863 189–202.
- 864 Grilli, S.T., Oliver-Denzil, S.T., Baxter, D.P., Marezki, S., 2009. A probabilistic approach for
865 determining submarine landslide tsunami hazard along the upper east coast of the United
866 States. *Marine Geology* 264, 74–97.
- 867 Great Barrier Reef Marine Park Authority, 2011. Impacts of tropical cyclone Yasi on the
868 Great Barrier Reef: a report on the findings of a rapid ecological impact assessment,
869 GBRMPA, Townsville.
- 870 Haflidason, H., Sejrup, H.P., Berstad, I.M., Nygard, A., Richter, T., Lien, R., Berg, K., 2003.
871 A weak layer feature on the northern Storegga slide escarpment. In: Miener, J., Weaver,
872 P.P.E. (Eds), *European margin sediment dynamics*, pp. 55–62, Springer.
- 873 Haflidason, H., Sejrup, H.P., Nygard, A., Mienert, J., Bryn, P., Lien, R., Forsberg, C.F., Berg,
874 K., Masson, D., 2004. The Storegga Slide: architecture, geometry and slide development.
875 *Marine Geology* 213, 201–234.
- 876 Harders, R., Kutterolf, S., Hensen, C., Moerz, T., Brueckmann, W., 2010. Tephra layers: A
877 controlling factor on submarine translational sliding? *Geochemistry, Geophysics,*
878 *Geosystems* 11, Q05S23, doi:10.1029/2009GC002844
- 879 Harders, R., Ranero, C., Weinrebe, W., Behrmann, J.H., 2011. Submarine slope failures along
880 the convergent continental margin of the Middle America Trench. *Geochemistry,*
881 *Geophysics, Geosystems* 12, Q05S32, doi:10.1029/2010GC003401

- 882 Hartin C.A., Fine R.A., Sloyan B.M., Talley L.D., Chereskin T.K., Happell J., 2011.
883 Formation rates of Subantarctic mode water and Antarctic intermediate water within the
884 South Pacific. *Deep-Sea Research I* 58, 524–534.
- 885 Hine, A. C., Locker, S. D., Tedesco, L. P., Mullins, H. T., Hallock, P., Belknap, D. F.,
886 Gonzales, J. L., Neuman, A. C., Snyder, S. W., 1992, Megabreccia shedding from modern,
887 low-relief carbonate platforms, Nicaraguan Rise. *Geological Society of America Bulletin*
888 104, 928–943.
- 889 Hinestrosa, G., Webster, J. M., and Beaman, R., 2016. Postglacial sediment deposition along
890 a mixed carbonate-siliciclastic margin: new constraints from the drowned shelf-edge reefs
891 of the Great Barrier Reef, Australia. *Palaeogeography Palaeoclimatology Palaeoecology*
892 446, 168–185.
- 893 Hogan, K.A., Dowdeswell, J.A., Mienert, J., 2013. New insights into slide processes and
894 seafloor geology revealed by side-scan imagery of the massive Hinlopen Slide, Arctic
895 Ocean margin. *Geo-Marine Letters* 33, 325–343.
- 896 Hughes-Clarke, J., 1994. Toward remote seafloor classification using the angular response of
897 acoustic backscattering: a case study from multiple overlapping GLORIA data. *IEEE*
898 *Journal of Ocean Engineering* 19, 364–374.
- 899 Hühnerbach, V., Masson, D.G., partners of the COSTA-Project, 2004. Landslides in the
900 North Atlantic and its adjacent seas: an analysis of their morphology, setting and behavior.
901 *Marine Geology* 213, 343–362.
- 902 Huvenne, V.A.I., Croker-Peter, F., Henriët, J.P., 2002. A refreshing 3D view of an ancient
903 sediment collapse and slope failure. *Terra Nova* 14, 33–40.
- 904 Huvenne, V.A.I., De Mol, B., Henriët, J.-P., 2003. A 3D seismic study of the morphology and
905 spatial distribution of buried coral banks in the Porcupine Basin, SW of Ireland. *Marine*
906 *Geology* 198, 5–25.
- 907 Huvenne, V.A.I., Van Rooij, D., DeMol, B., Thierens, M., O'Donnell, R., Foubert, A., 2009.
908 Sediment dynamics and palaeo-environmental context at keystages in the Challenger cold-
909 water coral mound formation: Clues from sediment deposits at the mound base. *Deep-Sea*
910 *Research I* 56, 2263–2280.
- 911 Iglesias, O., Lastras, G., Canals, M., Olabarrieta, M., González, M., Aniel-Quiroga, I., Otero,
912 L., Durán, R., Amblas, D., Casamor, J.L., Tahchi, E., Tinti, S., De Mol, B., 2012. The
913 BIG'95 Submarine Landslide-Generated Tsunami: A Numerical Simulation. *The Journal*
914 *of Geology* 120, 31–48.
- 915 Jo, A., Eberli, G.P., Grasmueck, M., 2015. Margin collapse and slope failure along
916 southwestern Great Bahama Bank. *Sedimentary Geology* 317, 43–52.
- 917 Kayen RE, Lee HJ (1991) Pleistocene slope instability of gas hydrate-laden sediment on the
918 Beaufort Sea margin. *Marine Geotechnology* 10, 125–141.

- 919 Kvenvolden, K. A. 1988. Methane hydrate—a major reservoir of carbon in the shallow
920 geosphere? *Chemical Geology* 71, 41–51.
- 921 Krastel, S., Wefer, G., Hanebuth, T.J.J., Antobreh, A.A., Freudenthal, T., Preu, B., Schwenk,
922 T., Strasser, M., Violante, R., Winkelmann, D., M78/3 shipboard scientific party, 2011.
923 Sediment dynamics and geohazards off Uruguay and the de la Plata River region (northern
924 Argentina and Uruguay). *Geo-Marine Letters* 31, 271–283.
- 925 Kvalstad, T.J., Andresen, L., Forsberg, C.F., Berg, K., Bryn, P., Wangen, M., 2005. The
926 Storegga slide: evaluation of triggering sources and slide mechanics. *Marine and*
927 *Petroleum Geology* 22, 245–256.
- 928 Laberg, J.S., Vorren, T.O., 2000. The Trænadjupet Slide, offshore Norway, morphology,
929 evacuation and triggering mechanisms. *Marine Geology* 171, 95–114.
- 930 Laberg, J.S., Vorren, T.O., Mienert, J., Haflidason, H., Bryn, P., Lien, R., 2003. Preconditions
931 leading to the Holocene Traenadjupet slide, offshore Norway. In: Locat, J., Mienert, J.
932 (Eds), *Submarine mass movements and their consequences*, pp. 247–254, Kluwer
933 Academic Publishers.
- 934 Lafuerza, S., Sultan, N., Canals, M., Lastras, G., Cattaneo, A., Frigola, J., Costa, S., Berndt,
935 C., 2012. Failure mechanisms of Ana Slide from geotechnical evidence, Eivissa Channel,
936 Western Mediterranean Sea. *Marine Geology* 307-310, 1–21.
- 937 Lastras, G., Canals, M., Hughes-Clarke, J.E., Moreno, A., DeBatist, M., Masson, D.G.,
938 Cochonat, P., 2002. Seafloor imagery from the BIG'95 debris flow, western
939 Mediterranean. *Geology* 30, 871–874.
- 940 Lastras, G., Canals, M., Urgeles, R., De Batist, M., Calafat, A.M., Casamar, J.L., 2004a.
941 Characterisation of a recent debris flow deposit on the Ebro margin, Western
942 Mediterranean Sea, after a variety of seismic reflection data. *Marine Geology* 231, 235–
943 255. Lastras, G., Canals, M., Urgeles, R., Hughes-Clarke, J.E., Acosta, J., 2004b. Shallow
944 slides and pockmark swarms in the Eivissa Channel, western Mediterranean Sea.
945 *Sedimentology* 51, 1–14.
- 946 Lastras, G., De Blasio, F.V., Canals, M., ElverhØi, 2005. Conceptual and numerical
947 modelling of the BIG'95 debris flow, western Mediterranean Sea. *Journal of Sedimentary*
948 *Research* 75, 784–797.
- 949 Lastras, G., Canals, M., Amblas, D., Ivanov, M., Dennielou, B., Droz, L., Akhmetzhanov, A.,
950 TTR-14 Leg 3 Shipboard Scientific Party, 2006. Eivissa slides, western Mediterranean
951 Sea: morphology and processes. *Geo-Marine Letters* 26, 225–233.
- 952 Lee, H.J., 2009. Timing of occurrence of large submarine landslides on the Atlantic Ocean
953 margin. *Marine Geology* 264, 53–64.
- 954 Lisiecki, L.E., Raymo, M.E., 2005. A Pliocene-Pleistocene stack of 57 globally distributed
955 benthic $\delta^{18}\text{O}$ records. *Paleoceanography* 20, PA1003. doi:10.1029/2004PA001071

- 956 Locat, J., Lee, H.J., 2002. Submarine Landslides: Advances and Challenges. Canadian
957 Geotechnical Journal 39, 193–212.
- 958 Masson, D.G., Watts, A.B., Gee, M.J.R., Urgeles, R., Mitchell, N.C., Le Bas, T.P., Canals,
959 M., 2002. Slope failures on the flanks of the western Canary Islands.
- 960 Matsumoto, T., Tappin, D.R., and SOS Onboard Scientific Party, 2003. Possible Coseismic
961 Large-scale Landslide off the Northern Coast of Papua New Guinea in July 1998:
962 Geophysical and Geological Results from SOS Cruises. Pure and Applied Geophysics 160,
963 1923–1943. McSaveney, M.J., Goff, J.R., Darby, D.J., Goldsmith, P., Barnett, A., Elliot, S.,
964 Nongkas, M. 2000. The 17 July 1998 tsunami, Papua New Guinea: evidence and initial
965 interpretation. Marine Geology 170, 81–92.
- 966 Mienis, F., van der Land, C., de Stigter, H.C., van de Vorstenbosch, M., de Haas, H., Richter,
967 T., van Weering, T.C.E., 2009. Sediment accumulation on a cold-water carbonate mound
968 at the Southwest Rockall Trough margin. Marine Geology 265, 40–50.
- 969 Moore, J.G., Clague, D.A., Holcomb, R.T., Lipman, P.W., Normark, W.R., Torresan, M.E.,
970 1989. Prodigious submarine landslides on the Hawaiian Ridge. Journal of Geophysical
971 Research 94, B12, 17465–17484.
- 972 Nissen, S.E., Haskell, N.L., Steiner, C.T., Coterill, K.L., 1999. Debris flow outrunner blocks,
973 glide tracks, and pressure ridges identified on the Nigerian continental slope using 3-D
974 seismic coherency. The Leading Edge 18, 595–599.
- 975 Normark, W.R., Piper, D.J.W., Sliter, R., 2006. Sea-level and tectonic control of middle to
976 late Pleistocene turbidite systems in Santa Monica Basin, offshore California.
977 Sedimentology 53, 867–897.
- 978 Owen, M., Day, S., Maslin, M., 2007. Late Pleistocene submarine mass movements:
979 occurrence and causes. Quaternary Science Reviews 26, 958–978.
- 980 Özeren, M.S., Çağatay, N., Postacıoğlu, N., Şengör, A.M.C., Görür, N., Eriş, K., 2010.
981 Mathematical modelling of a potential tsunami associated with a late glacial submarine
982 landslide in the Sea of Marmara. Geo-Marine Letters 30, 523–539.
- 983 Page, M.C., Dickens, G.R., Dunbar, G.B., 2003. Tropical view of Quaternary sequence
984 stratigraphy: siliciclastic accumulation on slopes east of the Great Barrier Reef since the
985 Last Glacial Maximum. Geology 31, 1013–1016.
- 986 Perry, C.T., Smithers, S.G., Kench, P.S., Pears, B., 2014. Impacts of Cyclone Yasi on
987 nearshore, terrigenous sediment-dominated reefs of the central Great Barrier Reef,
988 Australia. Geomorphology 222, 92–105.
- 989 Piper, D.J.W., Cochonat, P., Morrison, M., 1999. The sequence of events around the epicentre
990 of the 1929 Grand Banks earthquake: Initiation of debris flows and turbidity currents
991 inferred from sidescan sonar. Sedimentology 46, 79–97.

- 992 Posamentier, H.W., Vail, P.R., 1988. Eustatic control on clastic deposition II – sequence and
 993 system tracts models. In: Wilgus, C.K., Hastings, B.S., Posamentier, H., Van Wagoner, J.,
 994 Ross, C.A., Kendall, C.G.St.C. (Eds.), *Sea Level Changes: an Integrated Approach*, SEPM
 995 Special Publication 42, pp. 125–154.
- 996 Posamentier, H.W., Erksine, R.D., 1991. Seismic expression and recognition criteria of
 997 submarine fans. In: Weimer, P., Link, M.H. (Eds.), *Seismic facies and sedimentary
 998 processes of submarine fans and turbidite systems*, New York, Springer-Verlag, pp. 197–
 999 222.
- 1000 Principaud, M., Mulder, T., Hervé Gillet, Borgomano, J., 2015. Large-scale carbonate
 1001 submarine mass-wasting along the northwestern slope of the Great Bahama Bank
 1002 (Bahamas): Morphology, architecture, and mechanisms. *Sedimentary Geology* 317, 27–42.
- 1003 Prior, D.B., Doyle, E.H., Neurauter, T., 1986. The Currituck Slide, Mid-Atlantic continental
 1004 slope–revisited. *Marine Geology* 73, 25–45.
- 1005 Puga-Bernabéu, Á., Webster, J.M., Beaman, R.J., Guilbaud, V., 2011. Morphology and
 1006 controls on the evolution of a mixed carbonate-siliciclastic submarine canyon system,
 1007 Great Barrier Reef margin, north-eastern Australia. *Marine Geology* 289, 100–116.
- 1008 Puga-Bernabéu, Á., Webster, J.M., Beaman, R.J., 2013a. Potential collapse of the upper slope
 1009 and tsunami generation on the Great Barrier Reef margin, north-eastern Australia. *Natural
 1010 Hazards* 66, 557–575.
- 1011 Puga-Bernabéu, Á., Webster, J.M., Beaman, R.J., Guilbaud, V., 2013b. Variation in canyon
 1012 morphology on the Great Barrier Reef margin, north-eastern Australia: the influence of
 1013 slope and barrier reefs. *Geomorphology* 191, 35–50.
- 1014 Puga-Bernabéu, Á., Webster, J.M., Beaman, R.J., Reimer, P.J., Renema, W., 2014. Filling the
 1015 gap: A 60 ky record of mixed carbonate-siliciclastic turbidite deposition from the Great
 1016 Barrier Reef. *Marine and Petroleum Geology* 50, 40–50.
- 1017 Puga-Bernabéu, Á., López-Cabrera, F.J., Webster, J.M., Beaman, R.J., 2016. Submarine
 1018 landslides on the Great Barrier Reef margin, north-eastern Australia: Preliminary
 1019 characterization of their morphology and behaviour. 35th International Geological
 1020 Congress, 27th August–2nd September 2016, Cape Town, South Africa.
- 1021 Puotinen, M., 2004. Mapping tropical cyclone disturbance of the Great Barrier Reef. *The
 1022 Globe* 55, 31–41.
- 1023 Puzrin, A.M., Saurer, E., Germanovich, L.N., 2010. A dynamic solution of the shear band
 1024 propagation in submerged landslides. *Granular Matter* 12, 253–265.
- 1025 Ramprasad, T., Dewangan, P., Ramana, M.V., Mazumdar, A., Karisiddaiah, S.M., Ramya,
 1026 E.R., Sriram, G., 2011. Evidence of slumping/sliding in Krishnae–Godavari offshore basin
 1027 due to gas/fluid movements *Marine and Petroleum Geology* 28, 1806–1816.

- 1028 Reimer, P.J., Bard, E., Bayliss, A., Beck, J.W., Blackwell, P.G., Ramsey, C.B., Buck, C.E.,
 1029 Cheng, H., Edwards, R.L., Friedrich, M., Grootes, P.M., Guilderson, T.P., Haflidason, H.,
 1030 Hajdas, I., Hatte, C., Heaton, T.J., Hoffmann, D.L., Hogg, A.G., Hughen, K.A., Kaiser,
 1031 K.F., Kromer, B., Manning, S.W., Niu, M., Reimer, R.W., Richards, D.A., Scott, E.M.,
 1032 Southon, J.R., Staff, R.A., Turney, C.S.M., van der Plicht, J., 2013. INTCAL13 and
 1033 MARINE13 radiocarbon age calibration curves 0-50,000 years cal bp. *Radiocarbon* 55,
 1034 1869–1887.
- 1035 Rogers, K.G., Goodbred Jr, S.L., 2010. Mass failures associated with the passage of a large
 1036 tropical cyclone over the Swatch of No Ground submarine canyon (Bay of Bengal).
 1037 *Geology* 38, 1051–1054.
- 1038 Rohling, E.J., Foster, G.L., Grant, K.M., Marino, G., Roberts, A.P., Tamisiea, E., Williams,
 1039 F., 2014. Sea-level and deep-sea-temperature variability over the past 5.3 million years.
 1040 *Nature* 508, 477–482.
- 1041 Ruppel, C., 2007. Tapping methane hydrates for unconventional natural gas. *Elements* 3,
 1042 193–199, DOI: 10.2113/gselements.3.3.193.
- 1043 Russell, N., Cook, G.T., Ascough, P.L. Scott, E.M. Dugmore, A.J., 2011. Examining the
 1044 inherent variability in ΔR : New methods of presenting ΔR values and implications for
 1045 MRE studies. *Radiocarbon*, 53, 277–288.
- 1046 Sahal, A., Lemahieu, A., 2011. The 1979 Nice airport tsunami: mapping of the flood in
 1047 Antibes. *Natural Hazards* 56 (3), 833–840.
- 1048 Savini, A., Marchese, F., Verdicchio, G., Vertino, A., 2016. Submarine Slide Topography and
 1049 the Distribution of Vulnerable Marine Ecosystems: A Case Study in the Ionian Sea
 1050 (Eastern Mediterranean). In: Lamarche, G., Mountjoy, J., Bull, S., Hubble, T., Krastel, S.,
 1051 Lane, E., Micallef, A., Moscardelli, L., Mueller, C., Pecher, I., Woelz, S. (Eds.),
 1052 Submarine mass movements and their consequences, *Advances in Natural and*
 1053 *Technological Hazards Research* 41, 163–170.
- 1054 Scarselli, N., McClay, K., Elders, C., 2013. Submarine Slide and Slump Complexes, Exmouth
 1055 Plateau, NW Shelf of Australia. *The Sedimentary Basins of Western Australia IV:*
 1056 *Proceedings of the Petroleum Exploration Society of Australia Symposium, Perth, WA,*
 1057 *2013, pp. 1–20.*
- 1058 Smith, D.E., Harrison, S., Jordan, T., 2013. Sea-level rise and submarine mass failures on
 1059 open continental margins. *Quaternary Science Reviews* 82, 93–103. In: Keep, M., Moss,
 1060 S.J. (Eds), 2013, *The Sedimentary Basins of Western Australia IV: Proceedings of the*
 1061 *Petroleum Exploration Society of Australia Symposium, Perth, WA, 2013.*
- 1062 Solheim, A., Berg, K., Forsberg, C.F., Bryn, P., 2005. The Storegga Slide complex: repetitive
 1063 large scale sliding with similar cause and development. *The Storegga Slide complex:*
 1064 *repetitive large scale sliding with similar cause and development. Marine and Petroleum*
 1065 *Geology* 22, 97–107.

- 1066 Solokov S., Rintoul S.R., 2000. Circulation and water masses of the Southwest Pacific:
1067 WOCE Section P11, Papua New Guinea to Tasmania. *Journal of Marine Research* 58,
1068 223–268.
- 1069 Sterling, G.H., Strohbeck, G.E.. 1975. The Failure of South Pass 70B Platform in Hurricane
1070 Camille, *J. Petroleum Technology*, March 263–268.
- 1071 Strozyk, F., Strasser, M., Strasser, M., Krastel, S., Meyer, M., Huhn, K., 2010. Reconstruction
1072 of retreating mass wasting in response to progressive slope steepening of the northeastern
1073 Cretan margin, *eastern Mediterranean Marine Geology* 271, 44–54.
- 1074 Stuiver, M., Reimer, P. J., Reimer, R. W. 2005. CALIB 5.0 (program and documentation
1075 available at <http://calib.qub.ac.uk/calib>; accessed December 2016).
- 1076 Sultan, N., Cochonat, P., Foucher, J. P., Mienert, J., Haflidason, H., Sejrup, H. P. 2003. Effect
1077 of gas hydrates dissociation on seafloor slope stability. In: Locat, J., Mienert, J. (Eds.),
1078 Submarine mass movements and their consequences, Kluwer Academic Publishers, pp.
1079 103–111.
- 1080 Sultan, N., Cochonat, P., Canals, M., Cattaneo, A., Dennielou, B., Haflidason, H., Laberg,
1081 J.S., Long, D., Mienert, J., Trincardi, F., Urgeles, R., Vorren, T.O., Wilson, C., 2004a.
1082 Triggering mechanisms of slope instability processes and sediment failures on continental
1083 margins: a geotechnical approach. *Marine Geology* 213, 291–321.
- 1084 Sultan, N., Cochonat, P., Cayocca, F., Bourilet, J-F., Colliat, J-L., 2004b. Analysis of
1085 submarine slumping in the Gabon continental slope. *American Association of Petroleum*
1086 *Geologists* 88, 781–799.
- 1087 Sultan, N., Cochonat, P., Foucher, J.-P., Mienert, J., 2004c. Effect of gas hydrates melting on
1088 seafloor slope instability. *Marine Geology* 213, 379–401.
- 1089 Symonds, P. A., Davies, P. J., Parisi, A., 1983. Structure and stratigraphy of the central Great
1090 Barrier Reef. Bureau Mineral Resources, *Journal of Australian Geology and Geophysics*
1091 8, 277–291.
- 1092 Synolakis, C.E., Bardet, J-P., Borrero, J.C., Davies, H.L., Okal, E.A., Silver, E.A., Sweet, S.,
1093 Tappin, D.R., 2002. The slump origin of the 1998 Papua New Guinea Tsunami.
1094 *Proceedings of the Royal Society, London* 458, 763–789.
- 1095 Tappin, D.R., Watts, P., McMurtry, G.M., Lafoy, Y., Matsumoto, T., 2001. The Sissano,
1096 Papua New Guinea tsunami of July 1998 – evidence on the source mechanism. *Marine*
1097 *Geology* 175, 1–23.
- 1098 Tappin, D.R., McNeil, L.C., Henstock, T., Mosher, D.C., 2007. Mass wasting processes –
1099 offshore Sumatra. In: Lykousis, V., Sakellariou, D., Locat, J. (Eds.), *Submarine mass*
1100 *movements and their consequences: Advances in natural and technological hazards*
1101 *research*. Springer, pp. 327–337.

- 1102 Ten Brink, U.S., Geist, E.L., Andrews, B.D., 2006. Size and distribution of submarine
1103 landslides and its implications to tsunami hazard in Puerto Rico. *Geophysical Research*
1104 *Letters* 33, L11307, doi:10.1029/2006GL026125, 2006
- 1105 Tilbrook, B., Matear, R., 2009. Carbon Chemistry of the Great Barrier Reef. In: CSIRO (Ed),
1106 CSIRO Marine National Facility, Hobart, Australia, p. 17.
- 1107 Todorovska, M.I., Hayir, A., Trifunac, M.D., 2002. A note on tsunami amplitudes above
1108 submarine slides and slumps. *Soil Dynamics and Earthquake Engineering* 22, 129–141.
- 1109 Tournadour, E., Mulder, T., Borgomano, J., Hanquiez, V., Ducassou, E., Gillet, H., 2015.
1110 Origin and architecture of a Mass Transport Complex on the northwest slope of Little
1111 Bahama Bank (Bahamas): Relations between off-bank transport, bottom current
1112 sedimentation and submarine landslides. *Sedimentary Geology* 317, 9–26.
- 1113 Trifunac, M.D., Hayir, A., Todorovska, M.I., 2002. A note on the effects of nonuniform
1114 spreading velocity of submarine slumps and slides on the near-field tsunami amplitudes.
1115 *Soil Dynamics and Earthquake Engineering* 22, 167–180.
- 1116 Twichell, D.C., Chaytor, J.D., ten Brink, U.S., Buczkowski, B., 2009. Morphology of late
1117 Quaternary submarine landslides along the U.S. Atlantic continental margin. *Marine*
1118 *Geology* 264, 4–15.
- 1119 Urgeles, R., Leynaud, D., Lastras, G., Canals, M., Mienert, J., 2006. Back-analysis and failure
1120 mechanisms of a large submarine slide on the Ebro slope, NW Mediterranean. *Marine*
1121 *Geology* 226, 185–206.
- 1122 Urlaub, M., Talling, P.J., Masson, D.G., 2013. Timing and frequency of large submarine
1123 landslides: implications for understanding triggers and future geohazard. *Quaternary*
1124 *Science Reviews* 72, 63–82.
- 1125 Vanneste, M., Mienert, J., Bünz, S., 2006. The Hinlopen Slide: A giant, submarine slope
1126 failure on the north Svalbard margin, Arctic Ocean. *Earth and Planetary Science Letters*
1127 245, 373–388.
- 1128 Viana, A.R., Faugeres, J.C., Kowsmann, R.O., Lima, J.A.M., Caddah, L.F.G., Rizzo, J.G.,
1129 1998. Hydrology, morphology and sedimentology of the Campos continental margin,
1130 offshore Brazil. *Sedimentary Geology* 115, 133–157.
- 1131 Völker, D., Scholz, F., Geersen, J., 2011. Analysis of submarine landsliding in the rupture
1132 area of the 27 February 2010 Maule earthquake, Central Chile. *Marine Geology* 288,
1133 79–89.
- 1134 Von Huene, R., Ranero, C.R., Watts, P., 2004. Tsunamigenic slope failure along the middle
1135 America trench in two tectonic settings. *Marine Geology* 203, 303–317.
- 1136 Watts, K.F., Varga, L.L., Feary, D.A., 1993. Origins, timing, and implications of Miocene to
1137 Pleistocene turbidites, debris flows, and slump deposits of the Queensland Trough,

- 1138 northeastern Australia (Site 823). In: McKenzie, J.A., Davies, P.J., Palmer-Julson, A.,
1139 Sarg, J.F. (Eds), Proceedings of the Ocean Drilling Program, Scientific Results, Vol. 133.
1140 Ocean Drilling Program, College Station, Texas, U.S.A., pp. 379–445.
- 1141 Webster, J.M., Davies, P. J., 2003. Coral variation in two deep drill cores: significance for the
1142 Pleistocene development of the Great Barrier Reef. *Sedimentary Geology* 159, 61–80.
- 1143 Webster, J.M., Davies, P.J., Beaman, R.J., Williams, S., Byrne, M., 2008. Evolution of
1144 drowned shelf edge reefs in the GBR: Implications for understanding abrupt climate
1145 change, coral reef response and modern deep water benthic habitats. In: CSIRO (Ed),
1146 CSIRO Marine National Facility, Hobart, Australia, p. 18.
- 1147 Webster, J.M., George, N.P.J., Beaman, R.J., Hill, J., Puga-Bernabéu, Á., Hinestrosa, G.,
1148 Abbey, E.A., Daniell, J., 2016. Submarine landslides on the Great Barrier Reef shelf edge
1149 and upper slope: a mechanism for generating tsunamis on the north-east Australian coast?
1150 *Marine Geology* 371, 120–129.
- 1151 Weisler, M.I., Hua, Q., Zhao, J., 2009. Late Holocene ^{14}C marine reservoir corrections for
1152 Hawai’i derived from U-series dated archaeological coral. *Radiocarbon* 51, 955–968.
- 1153 Wiemer, G., Kopf, A., 2015. Altered marine tephra deposits as potential slope failure planes?
1154 *Geo-Marine Letters* 35, 305–314.
- 1155 Wheeler, A.J., Kozachenko, M., Henry, L.A., Foubert, A., de Haas, H., Huvenne, V.A.I.,
1156 Masson, D.G., Olu, K., 2011. The Moira Mounds, small cold-water coral banks in the
1157 Porcupine Seabight, NE Atlantic: Part A—an early stage growth phase for future coral
1158 carbonate mounds? *Marine Geology* 282, 53–64.
- 1159 Wolinsky, M.A., Pratson, L.F., 2007. Overpressure and slope stability in prograding
1160 clinoforms: Implications for marine morphodynamics. *Journal of Geophysical Research*
1161 112, F04011, doi:10.1029/2007JF000770.

1162

1163 **Figure captions**

1164 **Figure 1.** (A) Bathymetry 30 m DEM of the central part of the north-eastern Australia margin
1165 showing the location of the study area (yellow box inset) and main physiographic regions:
1166 Great Barrier Reef shelf and Queensland Trough. The slope is excavated by the Noggin
1167 Canyon system (Puga-Bernabéu et al., 2013b) and shows a large km-scale shelf indentation at
1168 the location of the Gloria Knolls Slide. Blue dots mark the position of the drilling sites of the
1169 Ocean Drilling Program Leg 133. Yellow dots mark the location of cores collected on RV
1170 *Franklin* Cruise FR4/92. Bathymetry contours in m. (B) Westerly view showing the Gloria
1171 Knolls Slide (GKS) and adjacent seafloor features. The GKS is divided into a source area at

1172 the slope (white dashed line) and a depositional area in the trough (pink dashed line). Yellow
1173 lines mark the location of sub-bottom seismic profiles shown in Fig. 5.

1174

1175 **Figure 2.** (A) Bathymetry 30 DEM of the study area showing the three main seafloor terrains
1176 that can be distinguished in the Gloria Knolls Slide based on seafloor morphology: the source
1177 area (SA), the proximal depositional area (PDA) and distal depositional area (DDA).
1178 Headwall scarps (hs) are marked with dashed lines. White lines with letters and black lines
1179 with numbers correspond to depth profiles shown in Fig. 3. (B) Slope gradient map. (C)
1180 Maximum slope direction (aspect). (D) Plan curvature map. (E) Profile curvature map. (F)
1181 Interpreted seafloor features.

1182

1183 **Figure 3.** Depth profiles (see Fig. 2A for location) corresponding to the reconstructed slope
1184 before the Gloria Knoll Slide (black) and present day slope (colour). h and h' indicate the
1185 range of maximum thickness of the slide mass.

1186

1187 **Figure 4.** Westerly view of the distal depositional area of the Gloria Knolls Slide complex
1188 showing the distribution of larger knolls and smaller debris blocks on the seafloor. The knolls
1189 are numbered from 1 to 8. Red numbers mark the location of the two depth profiles shown
1190 across knoll No. 1 and the smaller debris field. Note the presence of moats at the northern
1191 sides of the knolls. White star marks the position of the collected rock dredge on top of knoll
1192 No. 1.

1193

1194 **Figure 5.** TOPAS seismic sections over the depositional area of the Gloria Knolls Slide
1195 (GKS) complex (see Fig. 1B for location). Vertical scale is based on a sound velocity of 1550
1196 m s^{-1} (Davies et al., 1991a). (A) Across profile (main reflectors marked in colours) showing
1197 the sub-bottom character of the GKS deposit characterized by weak amplitude, transparent
1198 reflectors in the proximal depositional area (PDA), and more discontinuous and chaotic in the
1199 distal depositional area (DDA), where pressure-ridges are observed. The basal slide surface is
1200 not observed but notice the presence of blocks rising from deep positions. The GKS deposit is
1201 covered by a drape of hemipelagic sediment and alternating sediment gravity flow deposits
1202 (SGF) (continuous parallel to sub-parallel high amplitude reflectors bundled with low
1203 amplitude reflectors). A small-scale mass-transport deposit occurs close to the GKS headwall
1204 scarp. (B) Along profile (main reflectors marked in colours) showing the sub-bottom
1205 character of the GKS deposit. It includes two mass-transport deposits (M1 and M2)

1206 characterized by transparent reflectors. Note the presence of buried blocks rising from deep
1207 position, likely from the basal shear surface. The GKS deposits are covered by a drape of
1208 hemipelagic sediment and alternating sediment gravity flow deposits (C). Seismic line over
1209 knoll Nos. 1, 3, 7 and 8 and a buried block. Knolls are acoustically opaque and are draped
1210 with an up to 15 m thick hemipelagic sediment drape. Note the present of moats at the
1211 northern sides of the knolls.

1212

1213 **Figure 6.** Model of inception and evolution of the Gloria Knolls Slide (GKS) complex slope
1214 failure based on seafloor geomorphological analysis and sub-bottom seismic profiles (see text
1215 for details). Profiles to the right correspond to cross-section along dashed red line in the left-
1216 side drawings. Slope destabilization at water depths of the modern secondary headwall scarp
1217 generated the first failure event which left on the seafloor coherent blocks and disintegrated
1218 material, which were progressively covered with hemipelagic sediments. Subsequent failure
1219 events 2+3 removed significant areas of the slope and formed the main headwall scarp. Failed
1220 material in these two events progressively covered the seafloor irregularities and was
1221 compressed downslope forming pressure ridges. GKS scarps were subsequently re-shaped by
1222 gullies and canyons. More recent slope failures occur after the GKS, likely related to the gully
1223 upslope erosion. M1, M2 = mass-transport deposits. SGF = sediment gravity flow.

1224

1225 **Supplementary Figure 1.** Representative selection of fossil biota and lithified nodules taken
1226 from the dredge sample at top of knoll No. 1. Hand lens for scale is 8 cm long. See Figs. 1B
1227 and 4 for the dredge location.

1228

1229 **Supplementary Material 1.** Supplementary methods for U-Th dating.

1230

1231 **Supplementary Material 2.** Polyline shapefile showing 10 m contour interval multibeam
1232 bathymetry over the Gloria Knolls.

1233

Figure 1
[Click here to download high resolution image](#)

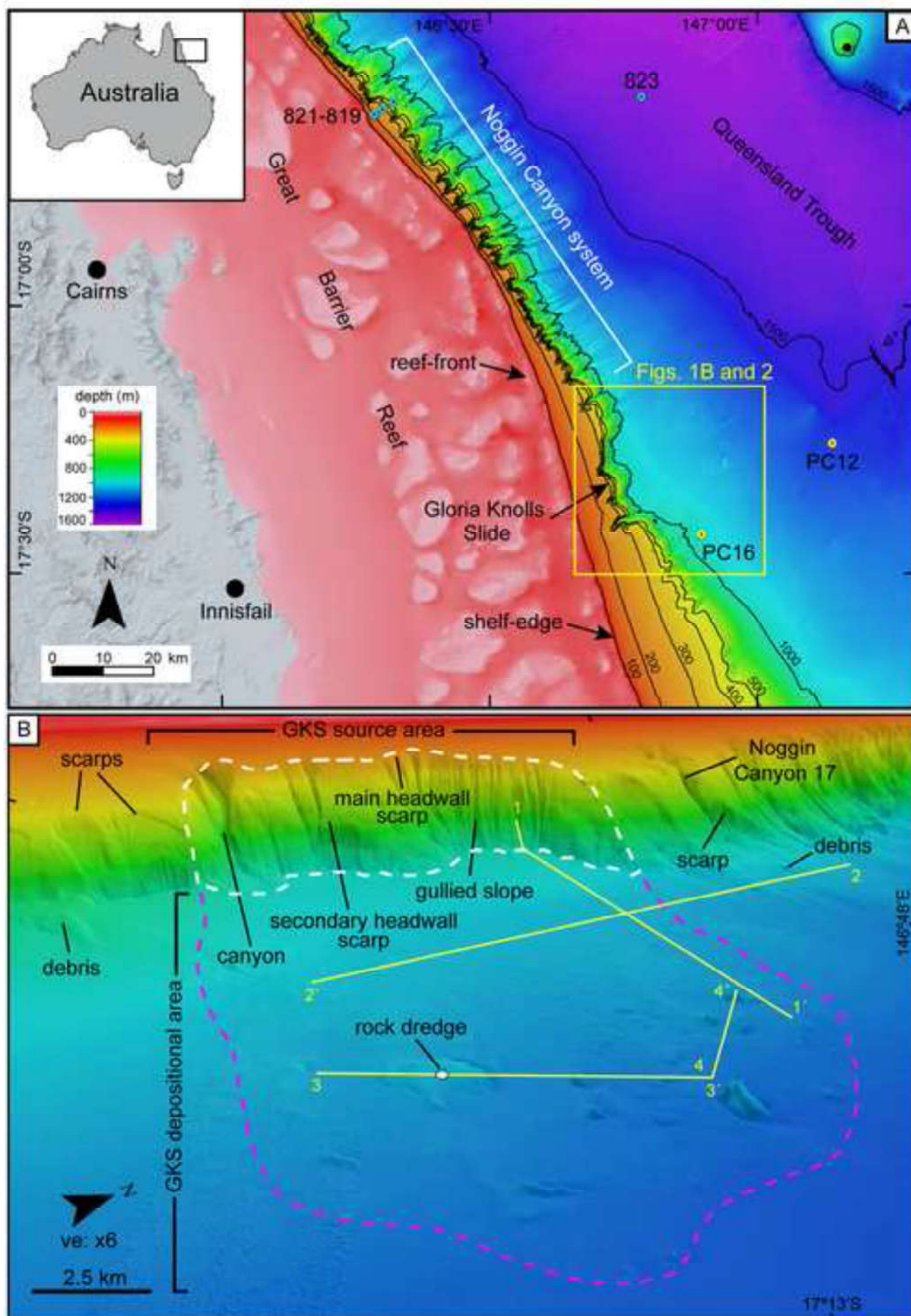


Figure 2
[Click here to download high resolution image](#)

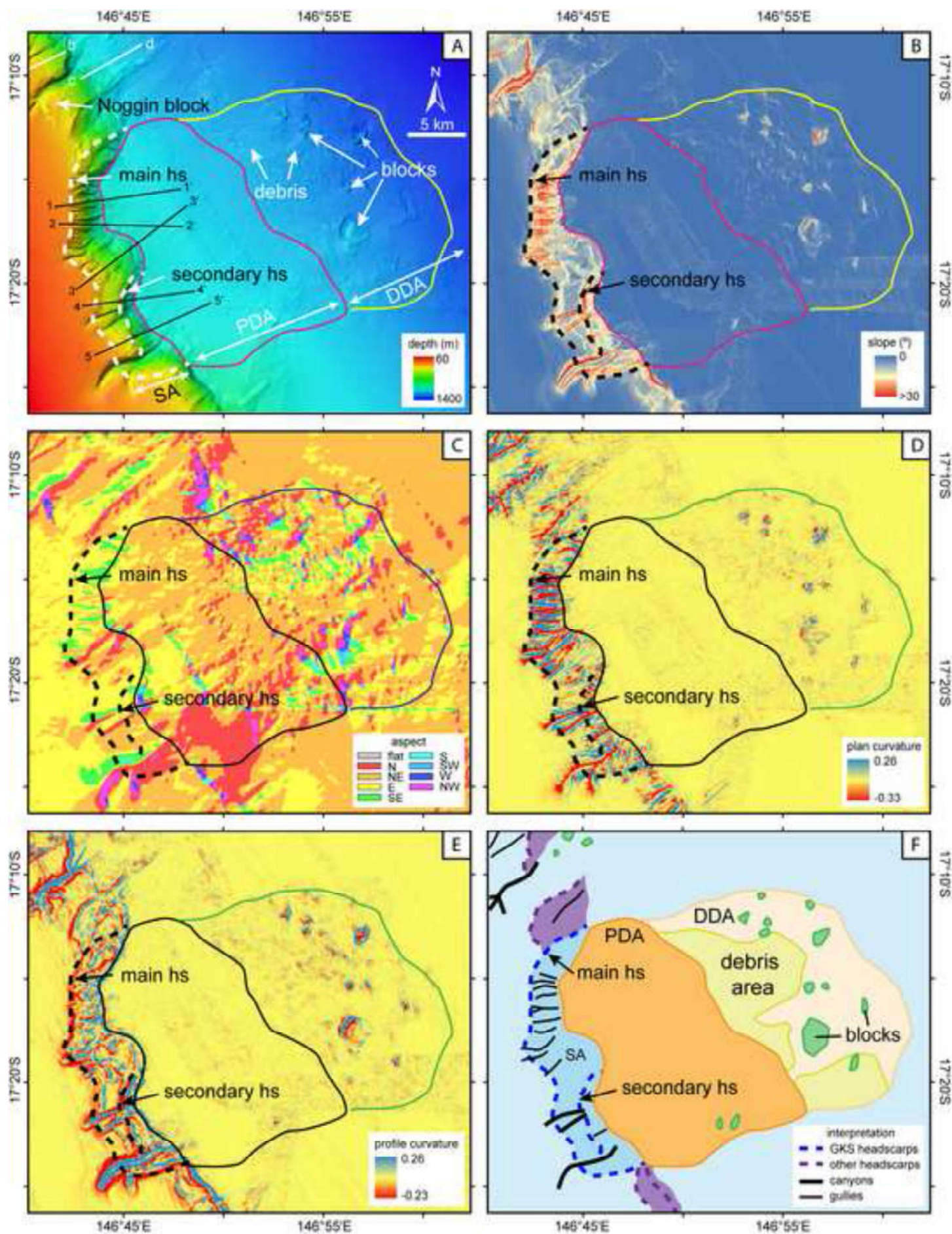
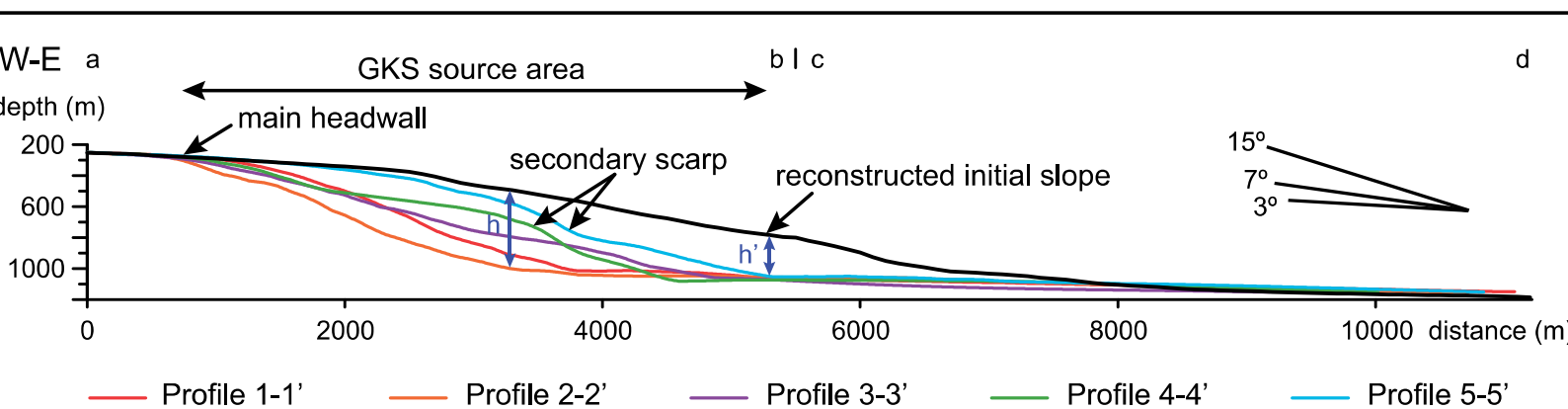


Figure 3



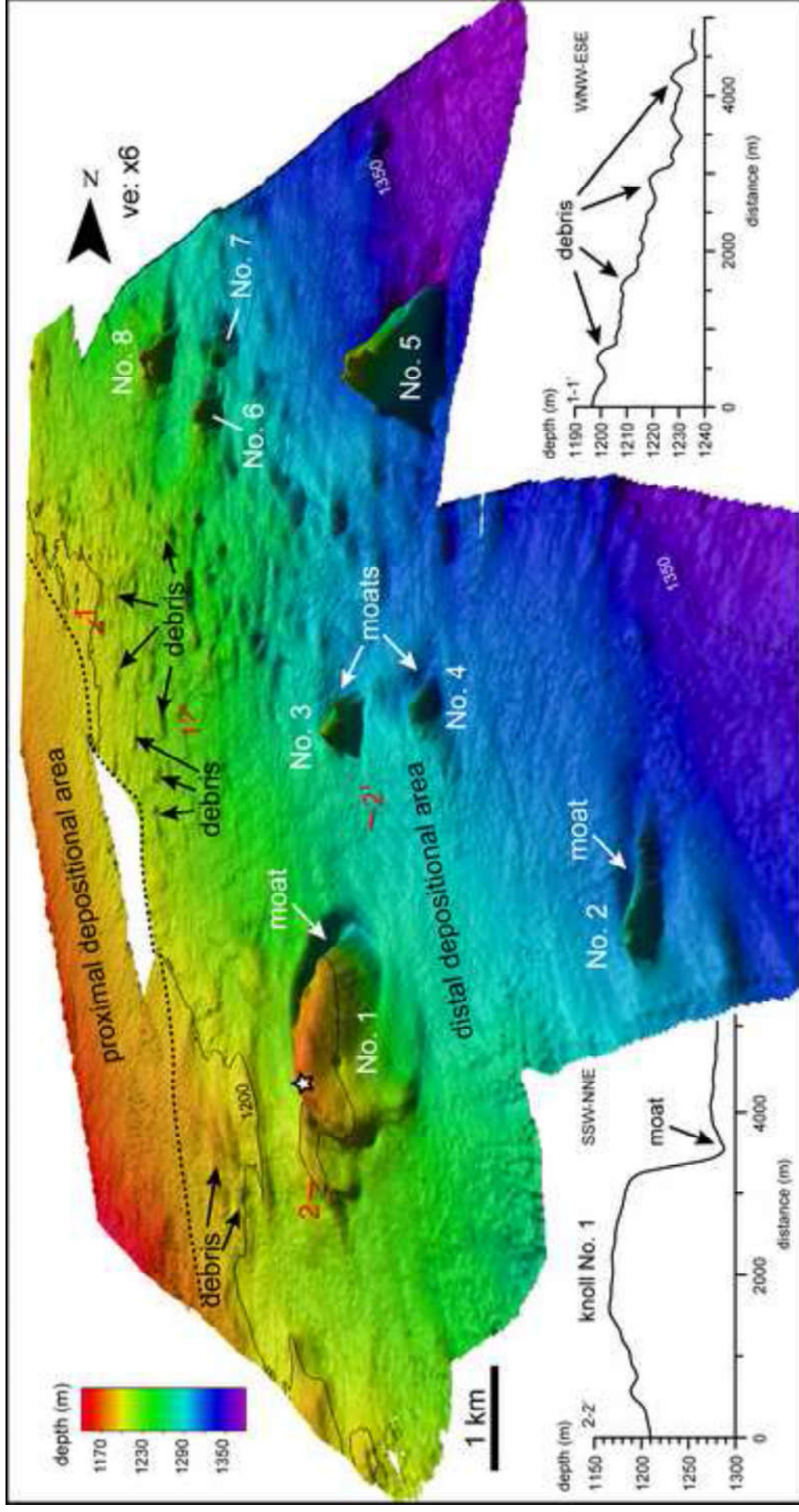


Figure 5
[Click here to download high resolution image](#)

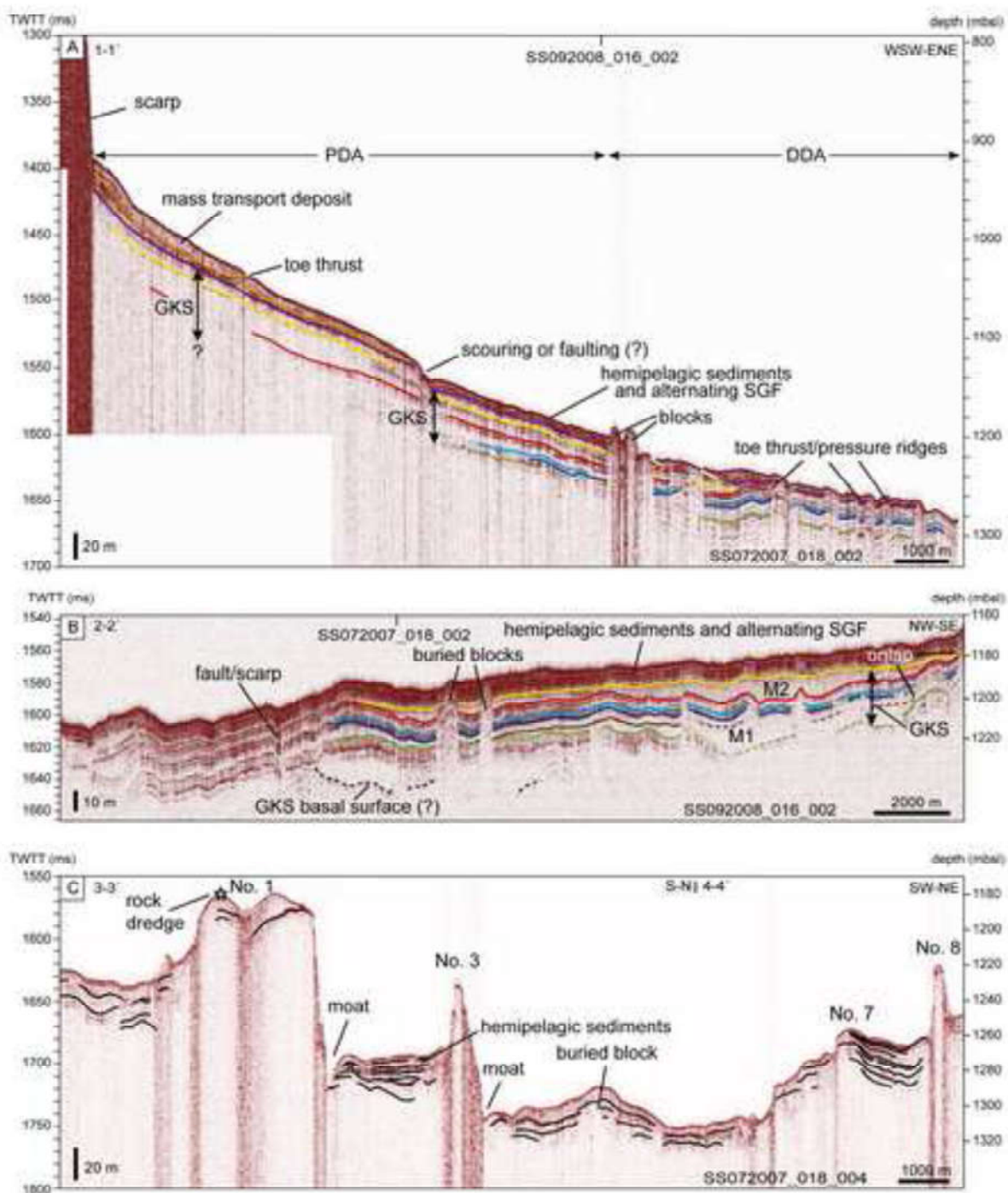
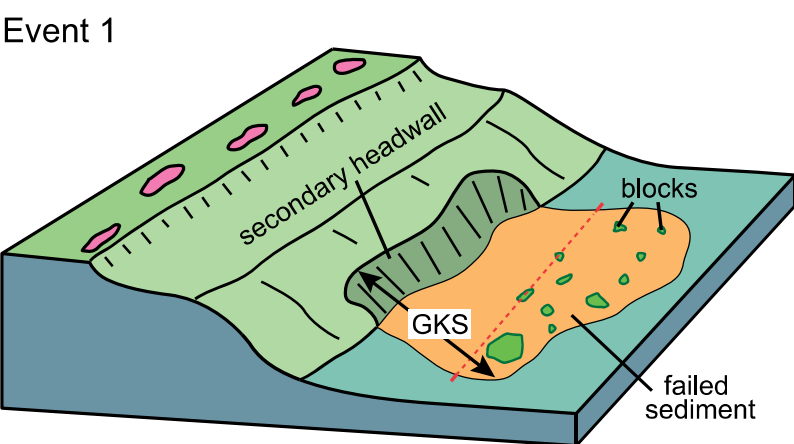
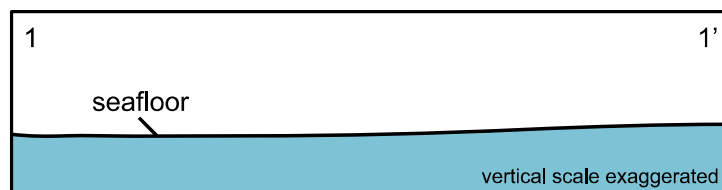
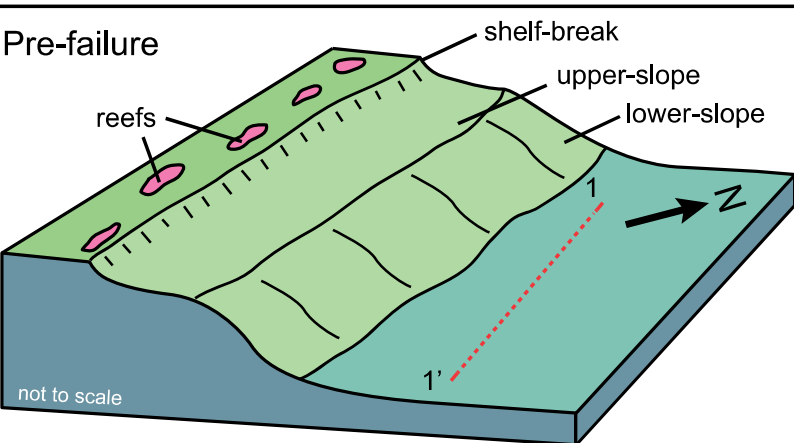
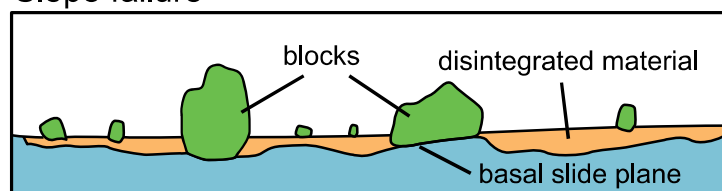


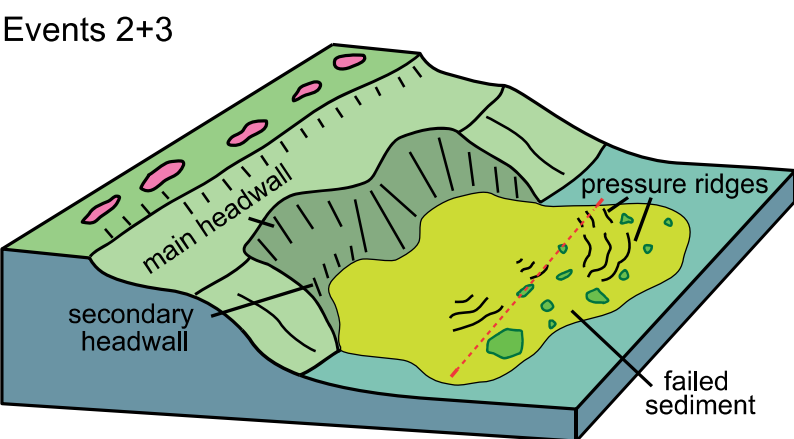
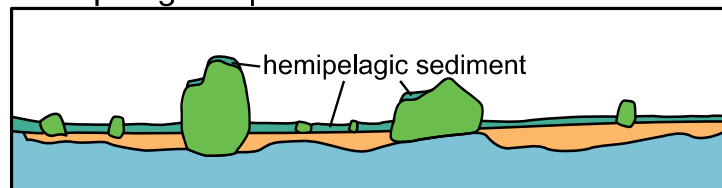
Figure 6



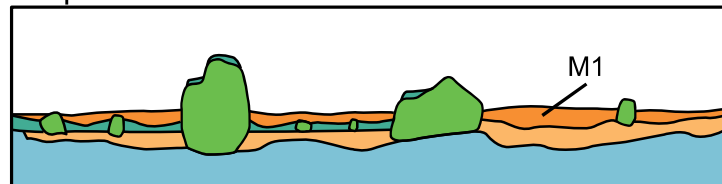
Slope failure



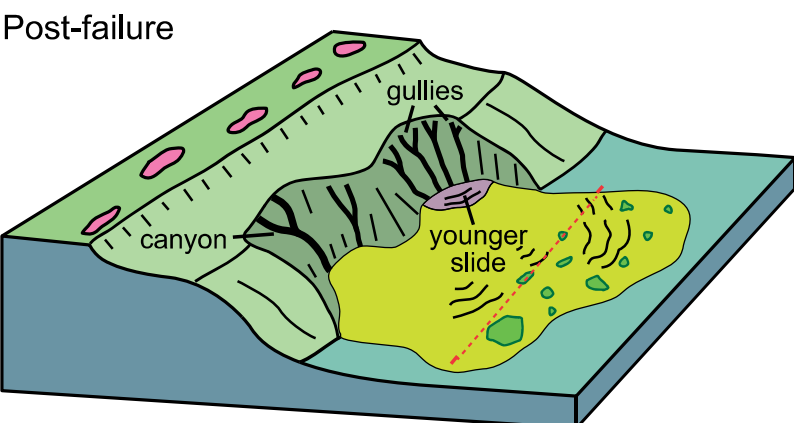
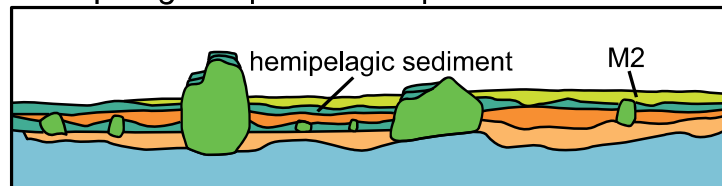
Hemipelagic deposition



Slope failure



Hemipelagic deposition-slope failure



Hemipelagic and alternating SGF deposition

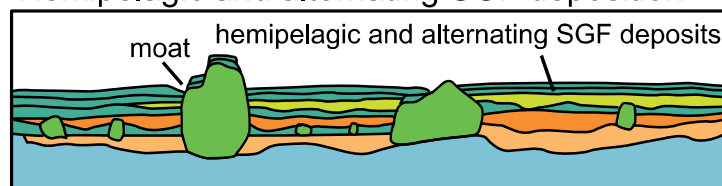


Table 1[Click here to download Table: Table 1.docx](#)**Table 1.** Parameters of the Gloria Knolls Slide complex.

Length (km): ~31
Width (km): ~ 20
Across slope source area width (km): ~ 8
Area (km ²): ~528
Area of slope removed ((km ²): ~174
Volume (km ³): ~32
Water depth source area (mbsl): 250 to 1050
Water depth deposition area (mbsl): ~1050 to 1350
Headwall height (m): 670 to 830
Headwall scarp gradient: 15° (average)
Unfailed adjacent slope gradient: 6-7° (average)
Estimated thickness of failed section (m): 260 to 500
Estimated thickness of the deposits (m): 17 to 37

Table 2[Click here to download Table: Table 2.docx](#)**Table 2.** Positions and dimensions of the Gloria Knolls within the distal depositional area (see Figs. 2 and 4).

No.	Latitude (South)	Longitude (East)	Max. length (km)	Min. width (km)	Area (km ²)	Min. depth (m)	Max. depth (m)	Height (m)
1	17°17.87'	146°56.30'	3.6	1.5	7.9	1165	1270	105
2	17°16.53'	146°59.08'	1.6	0.4	1.2	1268	1312	44
3	17°15.52'	146°56.29'	0.9	0.7	0.7	1226	1309	83
4	17°15.39'	146°57.16'	0.9	0.5	0.5	1265	1328	63
5	17°13.20'	146°56.75'	1.9	1.3	2.1	1196	1375	179
6	17°12.80'	146°54.13'	0.7	0.5	0.6	1215	1280	65
7	17°12.35'	146°54.23'	0.9	0.6	0.8	1245	1316	71
8	17°12.05'	146°53.01'	1.2	0.8	1.5	1189	1258	69

Table 3[Click here to download Table: Table 3.docx](#)**Table 3.** Sediment sample analysis for CNS, size classes and XRD results.

Sample type	Nitrogen weight %	Carbon weight %	Sulfur weight %	CaCO ₃ weight %	Mud vol %	Sand vol %	Gravel vol %	Carbonates weight %	Quartz weight %	Clays weight %
soft mud	0.03	6.56	0.04	54.67	59.62	40.38	0.00	82.2	7.9	10.0
semi-lithified nodule	0.03	9.34	0.03	77.87	67.52	32.48	0.00	78.1	8.4	13.6
lithified nodule	0.02	10.55	0.03	87.92	NA	NA	NA	83.5	8.6	7.8

Table 4. AMS and U-Th ages from fossil samples recovered from the Gloria Knoll No. 1 at 1170 m water depth (see Figs. 1B and 4 for location).

ANSTO lab code	Sample code	Sample name	Radiocarbon age kyr BP	1 σ error kyr	Calibrated age cal kyr BP (2 σ)	Calibrated Age cal kyr BP (2 σ)	U-Th age yr BP	2 σ error yr
OZL546	bamboo coral 1	unknown sp.	19.10	0.09	21.34 \pm 0.37	20.98-21.71		
OZL547	scleractinian coral 1	<i>Enallopsammia</i> sp.	51.90	1.10	Not calibrated	Not calibrated	301,899	19,105
OZL548	scleractinian coral 2	<i>Enallopsammia rostrata</i>	2.56	0.04	1.07 \pm 0.16	0.91-1.23	1,066	34
OZL549	scleractinian coral 3	<i>Madrepora oculata</i>	2.28	0.04	0.78 \pm 0.14	0.65-0.93	914	306
OZL550	gastropod 1	<i>Calliotropis pagodiformis</i>	26.83	0.16	29.47 \pm 0.52	28.95-29.99		
OZL551	gastropod 2	<i>Pontiohauma</i> sp.	5.40	0.05	4.52 \pm 0.26	4.26-4.78		
OZL552	coral on semi-lith. nodule	unknown sp.	5.08	0.04	4.06 \pm 0.23	3.82-4.29		
OZL553	coral on lith. nodule	unknown sp.	8.59	0.05	8.00 \pm 0.18	7.82-8.18		
OZL554	lithified nodule		44.78	0.64	46.66 \pm 1.34	45.32-48.01		
OZL555	barnacle 1	<i>Scillaelepas fosteri</i>	3.25	0.04	1.79 \pm 0.19	1.59-1.98		
OZL556	barnacle 2	<i>Scillaelepas fosteri</i>	2.54	0.04	1.06 \pm 0.16	0.89-1.23		
OZL557	pteropod	<i>Cavolinia tridentata</i>	3.66	0.05	2.29 \pm 0.23	2.06-2.52		
OZL558	bamboo coral 2	unknown sp.	2.78	0.04	1.30 \pm 0.18	1.12-1.48		

Calibrated against the Marine13 calibration curve (Reimer et al., 2013) using CALIB7.1 (Stuiver et al., 2005), with an estimated $\Delta R = 1,045 \pm 75$ ^{14}C yrs BP

Supplementary Figure 1

[Click here to download Supplementary Materials: Supplementary Figure 1.tif](#)

Supplementary Material 2

[Click here to download Supplementary Materials: GloriaKnolls_contour10m.dbf](#)

Supplementary Material 1

[Click here to download Supplementary Materials: Supplementary Material 1.docx](#)

Supplementary Material 2

[Click here to download Supplementary Materials: GloriaKnolls_contour10m.prj](#)

Supplementary Material 2

[Click here to download Supplementary Materials: GloriaKnolls_contour10m.sbn](#)

Supplementary Material 2

[Click here to download Supplementary Materials: GloriaKnolls_contour10m.sbx](#)

Supplementary Material 2

[Click here to download Supplementary Materials: GloriaKnolls_contour10m.shp](#)

Supplementary Material 2

[Click here to download Supplementary Materials: GloriaKnolls_contour10m.shp.xml](#)

Supplementary Material 2

[Click here to download Supplementary Materials: GloriaKnolls_contour10m.shx](#)